Materials Advances

ROYAL SOCIETY OF CHEMISTRY

PAPER

View Article Online
View Journal

Cite this: DOI: 10.1039/d6ma00193a

Ex situ modification of activated carbon through hydrothermal oxidation and sulphur@amine doping for highly efficient Pb^{2+} sorption: experimental and modelling approaches

Idris-Hermann Tiotsop Kuete, *[a] Cyrille Ghislain Fotsop, [b] Alexandra Lieb[b] and Franziska Scheffler*[b]

Lead ions present a multitude of dangers to human health and the ecosystem, even at very low concentrations. In this study, an *ex situ* approach was used to modify activated carbon (AC) derived from Garcinia kola nut shells. The AC was either directly modified by oxidation using $KMnO_4$, resulting in an oxidized form (AC-$KMnO_4$), or modified using an acid treatment leading to acid activated carbon (ACH), which was subsequently doped with sulfur and nitrogen using L-cysteine (ACH-L-cyst). The physico-chemical properties of ACH-L-Cyst and AC-$KMnO_4$ obtained using *ex situ* approach assisted hydrothermal oxidation, were evaluated by PXRD, FT-IR, SEM/EDX, Raman spectroscopy, and TGA/DTA analysis. The ability of the compounds to remove lead was assessed using batch sorption and mathematical modelling. The influence of four factors (pH, time, Pb^{2+} concentration and adsorbent mass) on the Pb^{2+} removal process was investigated using the central composite design approach. The experiments showed that the adsorption of Pb^{2+} by both adsorbents was favorable under the following optimum conditions: pH (5), equilibrium time (122.5 min), initial concentration (210 mg L^{-1}), and initial mass of adsorbent (60 mg), with a maximum adsorption capacity of 113 and 141 mg g^{-1} for ACH-L-Cyst and AC-$KMnO_4$, respectively. Pseudo-first order and pseudo-second order nonlinear kinetic models better describe the adsorption mechanism by highlighting the coexistence between physisorption and chemisorption on heterogeneous material surfaces. Adsorption isotherm data of ACH-L-Cyst and AC-$KMnO_4$ were best described by the non-linear model of Langmuir–Freundlich. According to the thermodynamic parameters, the adsorption reaction is endothermic ($\Delta H^\circ > 0$) and spontaneous ($\Delta G^\circ < 0$). The adsorbents showed high stability after six adsorption cycles, demonstrating the potential of these new materials for removing Pb^{2+} ions.

Received 11th February 2026,
Accepted 8th April 2026

DOI: 10.1039/d6ma00193a

rsc.li/materials-advances

1. Introduction

The proliferation of heavy metal contamination has become a pervasive global problem, with adverse effects on ecosystems and considerable threats to human health. Lead (Pb^{2+}) is particularly important in industrial applications, particularly in the automotive, emergency power and energy storage sectors.[1] However, activities such as printing, painting, mining, metallurgy and chemical manufacturing, as well as the production of lead batteries, result in the release of lead, which enters the human body *via* food webs. Lead contamination is increasingly recognised as a major environmental concern, as wastewater containing this metal is persistent, resistant to degradation and highly toxic.[2,3] It is important to note that lead is designated as a priority contaminant under the framework established by the U.S. Environmental Protection Agency (EPA), and the acceptable concentration of lead in drinking water should not exceed 10 μg L^{-1} [1,4] according to World Health Organization (WHO) guidelines.[1,5] Above this acceptable concentration, lead is recognized as a mutagenic and teratogenic element capable of inducing adverse toxicological effects on various biological systems, including the bone marrow, the nervous system, the renal system, and the immune system, with particular sensitivity observed in pediatric populations.[1,6,7] It is therefore becoming increasingly important and imperative to eradicate this category of pollutants from the aquatic ecosystem or to reduce their

[a] *Materials and Process Engineering Team, Research Unit of Noxious Chemistry and Environmental Engineering (RUNOCHEE), Department of Chemistry, Faculty of Science, University of Dschang, P. O. Box 67, Dschang, Cameroon. E-mail: hermann.kuete90@gmail.com*

[b] *Otto-von-Guericke-University Magdeburg, Chemical Institute, Chair for Industrial Chemistry, Universitätsplatz 2, 39106 Magdeburg, Germany. E-mail: franziska.scheffler@ovgu.de*

concentration before discharging them into the natural environment.

To this purpose, a wide variety of biological, chemical and physical methods are used and constantly refined to treat and recycle wastewater. It is clear from the scientific literature that there are a multitude of lead remediation methods are available, including reverse osmosis, membrane filtration, coagulation, ion exchange, precipitation, electrochemical deposition, photocatalysis, and adsorption.[8–12] Of the various methods listed, many approaches have inherent limitations, including inadequate removal systems, production of hazardous by-products, significant operational difficulties, economic inefficiencies, and excessive energy consumption. Conversely, adsorption is considered to be the most advantageous due to its superior removal efficiency, low operational costs, and ability to effectively separate a broad spectrum of pollutants present in industrial wastewater. The key to widespread application is to develop inexpensive and efficient adsorbents. In this particular context, a wealth of research has been carried out using adsorbent materials including biochar,[3,13,14] activated carbon,[15–17] lignocellulosic materials,[18,19] Metal–organic frameworks (MOFs).[10,20,21] It is imperative to recognize that the choice of adsorbents depends on several criteria, including their porosity, thermal and mechanical stability, flexibility, high specific surface area, the versatility of its production and regeneration capacity. Activated carbon (AC) is one of the adsorbents that meets most of these specified criteria, as its adsorption properties result from its internal porosity and the composition of its surface functional groups.

Recently, lignocellulosic materials have attracted increasing research attention, which offer advantages in terms of cost-effectiveness and renewability, and which could serve as precursors for the production of AC. The lignocellulosic materials used include: shrimp (*Penaeus monodon*) shells and *Cucumeropsis mannii* Naudin seed shells,[22] rubber seed hull,[16] cocoa pods,[17] Shea Residue (*Vitellaria paradoxa*),[23] walnut shell,[24] date palm (*Phoenix dactylifera* L.).[15] As part of this study, Cameroonian residual biomass from *garcinia cola* shells, was used as a precursor material for the production of oxidized activated carbon and sulfur- and nitrogen-doped activated carbon. The approach to modifying the adsorbents used in this study, which highlights next-generation technology, is rarely reported in the literature. However, several researchers have studied the elimination of lead using different materials. For example, Aloud *et al.* reported on the removal of Pb^{2+} using AC obtained using microwave-assisted K_2CO_3 activation of date Palm Leaf Sheath Fibers, with an removal capacity of 5.67 mg g^{-1} at pH 6.[15] However, Singh *et al.* reported on the adsorption of Pb^{2+} and Cd^{2+} in aqueous solutions using fly ash and TiO_2-modified form as adsorbent materials with a maximum adsorption capacity of 62.70 and 75.30 mg g^{-1} for Pb, respectively at 308 K.[25] Takele *et al.* reported on the adsorption of Pb^{2+} using AC derived from african arrowroot (*Canna indica*) Stem with a maximum adsorption capacity of 8.52 mg g^{-1} at pH 5.5.[11] Shanavaz *et al.* reported on the removal of Pb^{2+} ions using stable imine linked covalent organic frameworks, they showed that the adsorption capacity increased with the pH to 1–8, reaching a maximum adsorption capacity of 601.6 mg g^{-1} at pH 6.[4] Gao *et al.* investigated on the quantitative adsorption mechanisms of Pb by oxidized rape straw biochars. They showed that chemical oxidation is an effective way of improving the ability of biochar to remove metals. They showed that among the different oxidized biochars (using HNO_3, H_2O_2 and $KMnO_4$), the one oxidized with $KMnO_4$ adsorbs more Pb, with an adsorption capacity of 1343 mmol kg^{-1} at pH 2 and an initial concentration of 1.0 mol L^{-1}.[26] Zhu *et al.* reported on the removal of Pb^{2+} by AC fibers modified by L-cysteine, a maximum adsorption capacity of 179.53 mg g^{-1} at pH 6 was observed.[9] Mahmoud *et al.* reported on the removal of heavy metal ions from wastewater by polyvinyl alcohol-conjugated L-cysteine with a maximum adsorption capacity of 45.25 mg g^{-1} for Pb.[27] Amin *et al.* reported on the removal of Pb^{2+} and Cr^{3+} ions from contaminated water sources using poly iminophosphorane composite with a maximum adsorption capacity of 55 mg g^{-1} for Pb^{2+}.[28] Malitha *et al.* reported on the rapid adsorptive removal of Pb^{2+} ions from aqueous systems using a magnetic graphene oxide calcium alginate composite with a maximum adsorption capacity of 270.27 mg g^{-1}.[29] Nevertheless, successful removal of a contaminant requires consideration of all the variables influencing its adsorption.

The application of mathematical optimization techniques represents a significant methodological advance that guarantees the experimental reproducibility of all designated investigations. This methodology recognizes simultaneous interactions and quadratic effects that may not be readily observable by experimental means. To this end, the Response Surface Methodology (RSM) focuses primarily on a factorial design to determine optimal experimental parameters in line with regulatory standards, while reducing errors and minimizing the duration of all experimental procedures. Centered Composite design (CCD) enables simultaneous examination of experimental, optimization and interaction variables to effectively assess their impact on properties of interest in multivariate settings.

The main objective of this study is threefold: firstly, the doping of activated carbon surface with sulfur and nitrogen using L-cysteine by the solvothermal method under reflux heating and, secondly, the oxidation of activated carbon using $KMnO_4$ under magnetic stirring in an oil bath by the hydrothermal method. Finally, present an improved strategy for the use of the newly obtained materials in lead removal using a mathematical approach to optimize the adsorption conditions, namely pH, adsorbent mass, metal concentration, and adsorption time, followed by recyclability.

2. Reagents and methods

2.1. Reagents

The Garcinia cola shells used to prepare the activated carbon were collected in Mandjo, in the Moungo division of Cameroon's Littoral region. Chemical reagents such as concentrated

HNO_3 (70% purity), and H_3PO_4 (99% purity), $KMnO_4$ (99% purity), $Pb(NO_3)_2$ (99% purity), ethanol (99.9% purity), DMF (99.8% purity) NaOH (99% purity) and distilled water (DW) were used. All reagents were purchased from Sigma-Aldrich, expect for the DW.

2.2. Experimental protocol

2.2.1. Synthesis of ACH-L-Cyst and AC-$KMnO_4$ adsorbents using the *ex situ* approach. – Activated carbon preparation

Activated carbon (AC) was produced using the *in situ* approach of chemical activation: 300 g of crushed and dried biomass, with diameters ranging from 250 to 1000 μm, were mixed with 0.20 mol L^{-1} phosphoric acid (H_3PO_4) at a mass ratio of 1 : 1 (w/w) for impregnation, under magnetic stirring, for 24 hours. After impregnation, the resulting product was dried and placed in a porcelain crucible with a lid. It was then introduced into an ISUNU electric furnace for calcination in an oxygen-free environment at 500 °C for one hour, with a heating rate of 5 °C min^{-1}. After cooling to room temperature, the AC was washed several times with DW by vacuum filtration. The final product was then dried at 110 °C for 48 hours and named AC.

– Hydrothermal oxidation and solvothermal doping using sulphur@amine of AC

AC-$KMnO_4$ composite was synthesized by hydrothermal oxidation of AC using the *ex situ* approach. 4 g activated carbon, previously synthesized, were mixed with 250 mL of $KMnO_4$ solution (37% w_{KMnO_4}/w_{AC}, *i.e.* 1.5 g $KMnO_4$). The mixture was dispersed using an ultrasonic bath for 30 min, then kept under heated magnetic stirring at 50 °C for 6 hours. The resulting mixture was filtered under vacuum, and the composite obtained was washed with distilled water until a neutral solution was obtained and dried in an oven at 100 °C for 24 hours, then ground to obtain fine particles ≤100 μm.

ACH-L-Cyst composite was synthesized by doping S and N from L-cysteine onto AC activated carbon by the solvothermal method using an *ex situ* approach. 16 g of previously synthesized activated carbon were mixed with 250 mL of 1 mol L^{-1} phosphoric acid in a 500 mL round-bottomed flask. The mixture was stirred under reflux at 90 °C for 6 hours. The new material obtained was washed with DW using vacuum filtration until a clear filtrate was obtained, dried at 100 °C for 24 hours and then ground to fine particles. The resulting ACH-coded material was doped with L-cysteine by the solvothermal method. For this purpose, 2 g of ACH and 3 g of L-cysteine were added to 100 mL of DMF and stirred for 36 h under reflux at 80 °C. The resulting composite was filtered under vacuum and washed with distilled water to obtain a neutral pH filtrate. It was then oven-dried at 100 °C for 24 hours and ground into particles measuring ≤100 μm.

2.2.2. Adsorbents characterization. X-ray diffraction analysis of the adsorbents was carried out using an Empyrean diffractometer PAN Analytical Almelo, which is automated and operates with anode-filtered Cu-Kα radiation (λ: $K_{\alpha 1}$ = 1.540598 Å and $K_{\alpha 2}$ = 1.544426 Å) operating at 40 mA and 40 kV. All samples were scanned from 4–90° 2θ. Fourier transform infrared (FTIR) measurements were performed on a FTIR spectrometer (Thermo Scientific Nicolet iS50, USA) in the 4000–200 cm^{-1} range. Raman spectroscopy was carried out on a RAM HR evolution (Kyoto, Japan) using a monochromatic laser with an excitation energy of 532 nm. An FE-SEM (XL30 ESEM from FEI, Hillsboro, fitted with a Genesis energy dispersive X-ray detector from EDAX, Mahwah, USA) was used to evaluate the surface morphology. The TGA/DTA analysis was performed using a thermogravimetric analyzer (STA 449C Jupiter, Netzsch, Selb, Germany).

2.2.3. Adsorption experiments. The Pb^{2+} adsorption tests using different adsorbents were carried out at room temperature in a batch process. Different amounts of adsorbent and Pb^{2+} concentrations were measured; the pH of the solution was then adjusted, and the mixture was stirred according to each set of experiments. All tests were performed in a 100 mL beaker stirred on a magnetic stirrer at 500 rpm. Following filtration, a microwave plasma atomic emission spectroscopy (MP-AES, Meinhard, TR-30-K1, Serie 5975) was used to determine the residual concentration. Furthermore, every single factor study was carried out twice. The influence of contact time, concentration, temperature and interfering ions (Pb^{2+}, Sr^{2+}, Ni^{2+}, In^{2+}, Cu^{2+}, Ca^{2+}, Co^{2+} and Mg^{2+}) was studied using the previously determined optimum value of each factor while varying the contact time from 5 to 210 min, the concentration from 100 to 350 mg L^{-1}, and the temperature from 25 °C, 35 °C, and 45 °C. Eqn (1) and (2) were then used to calculate the adsorption capacity (Q_e) and adsorption efficiency (%R) of Pb^{2+} and each ion.

$$Q_{ads} = \frac{(C_0 - C_e)}{m} \times V \quad (1)$$

$$\%R = \frac{(C_0 - C_t)}{C_0} \times 100 \quad (2)$$

where C_t is the concentration at time t, C_e is the equilibrium concentration of the Pb^{2+}, C_0 is the beginning concentration, V the volume of solution and m is the mass of the adsorbent. The stages involved in ACH-L-Cyst and AC-$KMnO_4$ preparation and Pb^{2+} adsorption are presented in Fig. 1.

2.2.4. Designing experiments and optimization. A central composite design (CCD) was used to optimize the four factors: pH of solution (A), stirring time (B), initial metal concentration (C), and amount of each adsorbent (D) as independent variables and the percentage of Pb^{2+} ion adsorption as the response variable. Design Expert® software version 13.0.5.0 was used for experimental design for process optimization and statistical analysis, featuring 4 central points (Table S1, SI). According to eqn (3), the CCD generates 28 experiments.

$$N = 2^f + 2f + f_c = 2^4 + 2(4) + 4 = 28 \quad (3)$$

N represents the total number of experiments, f symbolizes the number of experimental variables and f_c designates the number of center points. The selection of the number of central points is crucial for the evaluation of experimental errors and the reproducibility of the results obtained. The 4 experimental

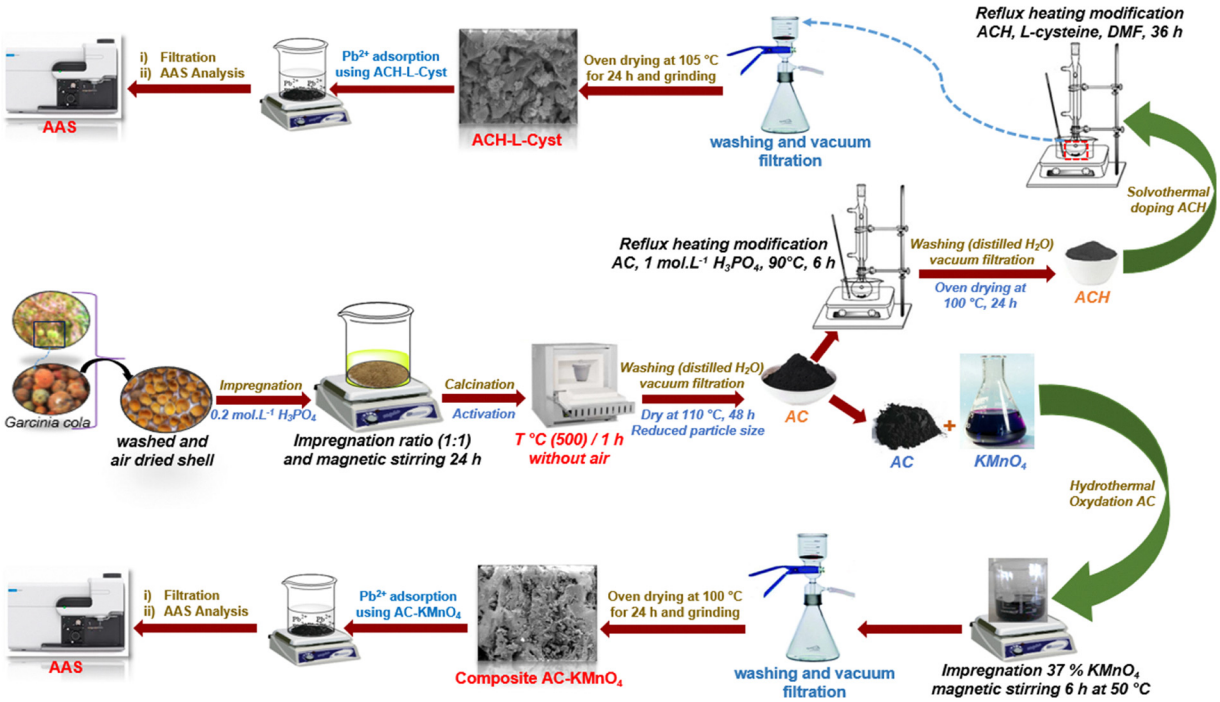

Fig. 1 Experimental methods for adsorbent synthesis and adsorption of Pb^{2+} ions.

factors are coded +1 and −1 for the minimum and maximum values, and 0 for the central value, as shown in Table 1.

The 28 experiments were randomized within blocks to minimize the impact of uncontrollable factors. For each series of experiments, the expected response was the amount of Pb^{2+} ions adsorbed. A quadratic polynomial equation (see eqn (4)) was developed based on the independent variables and their interactions, with the aim of establishing a link between the amount of Pb^{2+} ions adsorbed.

$$Z = \alpha_0 + \sum_{i=1}^{n} \alpha_i x_i + \sum_{i=1}^{n} \alpha_{ii} x_i^2 + \sum_{i=1}^{n} \sum_{j=1}^{n} \alpha_{ij} x_i x_j + \varepsilon \qquad (4)$$

where Z is the predicted response, α_0, α_{ii}, α_{ij} are the constant, quadratic and interaction coefficient, respectively. x_i and x_j are the coded values of the factors, and ε is the uncertainty between the measured and predicted values.

2.2.5. Isotherm, kinetic and error function analysis. The mechanisms involved in adsorption of Pb^{2+} ions on ACH-L-Cyst and AC-$KMnO_4$ were investigated using non-linear pseudo-first-order (PFO), pseudo-second-order (PSO), intra-particle diffusion and Elovich kinetic models. The mathematical expressions for these models are presented in Table S2. Adsorption isotherm are used to study how the metal ion is adsorbed by different adsorbents. To fit the equilibrium adsorption isotherm of Pb^{2+} ions, the non-linear isotherm models of Langmuir, Jovanovic, Temkin, Freundlich, Dubinin–Raduskevish, Langmuir–Freundlich and Redlich–Peterson were studied. The mathematical expressions for these models are presented in Table S3. The best fit of experimental kinetic and isotherm data was evaluated based on the values of R^2, χ^2, RMSE, ARE and SCE which were fitted using Origin 2019b program. The mathematical expressions for these models are presented in Table S4.

Table 1 Codification of experimental factors

Factors and coded variable	Coded level −1	0	+1
	Actual level		
pH: A	2	5	8
Time (min): B	5	122.5	240
Initial concentration (mg L^{-1}): C	20	210	400
Mass (mg): D	20	60	100

3. Results and discussion

3.1. Analysis of characterization

3.1.1. PXRD, FT-IR and Raman analysis. Fig. 2a shows the PXRD patterns of the different adsorbents. As shown, the AC, ACH, and AC-$KMnO_4$ adsorbents have amorphous structures, while the ACH-L-Cyst adsorbent has a crystalline structure. However, diffraction peaks observed at 2θ = 18.7, 28.2, 33.0, 34.4, and 38.2° reveal the crystalline nature of ACH-L-Cyst, an acidified activated carbon doped with sulfur and nitrogen using L-cysteine. This finding aligns with the results of Han *et al.* (2021),[30] who demonstrated that L-cysteine-functionalized NH_2-MIL-53(Al) exhibits a crystalline structure. The PXRD diffractogram of AC-$KMnO_4$ reveals two new peaks (d = 2.4 nm and d = 1.4 nm), which could correspond to amorphous MnO_2.[26] This finding agrees with that reported by Gao *et al.* (2019) when oxidizing biochars from rapeseed straw with $KMnO_4$.[26]

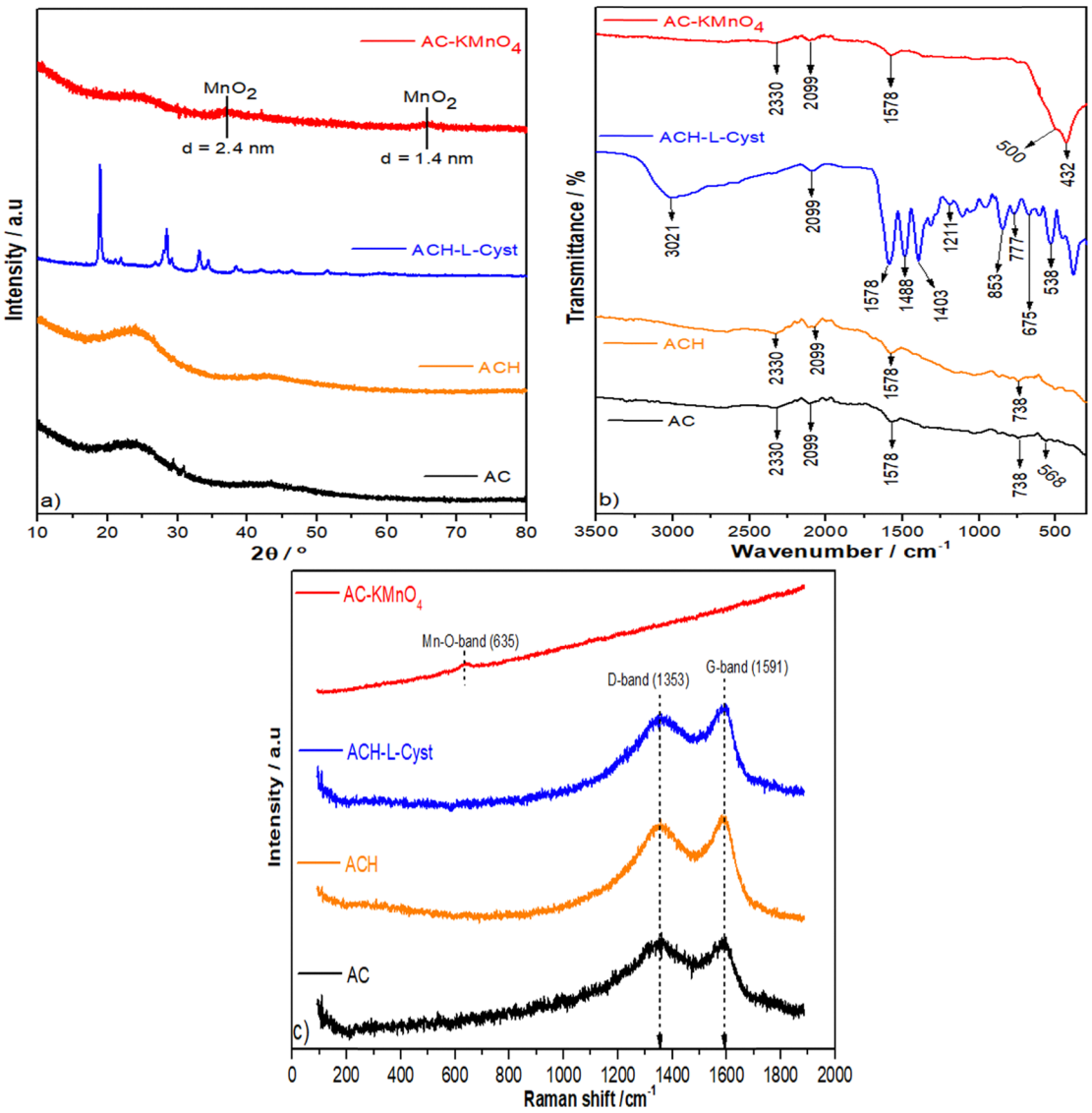

Fig. 2 PXRD pattern (a), FT-IR spectra (b) and Raman spectra (c).

Fig. 2b shows the FT-IR spectra of different adsorbents. As shown in this figure, the different bands in the spectra indicate the presence of various functional groups. Additional bands are observed in the infrared spectra of the modified adsorbents AC-$KMnO_4$ and ACH-L-Cyst. The ACH-L-Cyst spectrum shows the presence of L-cysteine in the form of a peak at 3021 cm^{-1}, attributed to the stretching vibration of the hydroxyl group (O–H).[31] The peak at 2330 cm^{-1} in the AC, ACH, and AC-$KMnO_4$ spectra is attributed to the C–H and C═O vibration absorption peaks of aldehydes/ketones.[32] The peak observed at 2099 cm^{-1} in the AC, ACH, and AC-$KMnO_4$ spectra can be attributed to the C–C stretching vibration of alkynes, C–N of nitriles, or C–N of cyanides. This peak may also indicate Mn–C interactions in the AC-$KMnO_4$ adsorbent. In the ACH-L-Cyst spectrum, the peak at 2099 cm^{-1} is attributed to the S–H stretching vibration of the thiol group. In the AC, ACH, and AC-$KMnO_4$ spectra, the peak at 1578 cm^{-1} is attributed to the stretching vibration of the aromatic ring's C═C–C and the C═O of the carbonyl group. In the ACH-L-Cyst spectrum, the peak at 1578 cm^{-1} can be attributed to the N–H absorption vibration of L-cysteine.[33] Similarly, the peaks observed at 1488, 1408, and 853 cm^{-1} are absent from the AC, ACH, and AC-$KMnO_4$ spectra and correspond, respectively, to C–O stretching vibrations, H–C–H bending vibrations, and the stretching vibration of the –CN group.[31] In the ACH-L-Cyst spectrum, the small peaks at 1211, 777, and 675 cm^{-1} are attributed to the C═S bond, the $-NH_2$ bending vibration, and the C–S bond vibration, respectively.[9] The peak at 538 cm^{-1} can likely be attributed to C–S stretching vibrations or C–H bond vibrations. In the AC-$KMnO_4$ spectrum, the peaks at 500 and 432 cm^{-1} can be attributed to stretching or bending vibrations of Mn–O and low-frequency vibrations of Mn–O. This shows that the $KMnO_4$ formed Mn–O bonds on the adsorbent surface or that there are vibrations of C–Mn bonds on the surface, respectively.

Fig. 2c shows the Raman spectra of different adsorbents. The Raman spectra of AC, ACH, and ACH-L-Cyst show two prominent peaks at 1353 cm^{-1} and 1591 cm^{-1}, which correspond to the D and G bands, respectively. The D peak indicates that all three adsorbents contain amorphous carbon atoms with structural anomalies corresponding to the characteristic peak of disordered carbon.[34] Peak G indicates that the sp^2 carbon atoms of all three adsorbents are hybridized, which corresponds to the characteristic peak of ordered graphite.[34] Peak G represents the graphitic configuration related to the $2E_{2g}$ mode of a two-dimensional network structure.[35] The intensity ratio of the D and G peaks, known as the I_D/I_G ratio, provides an overview of the material's structural characteristics. The I_D/I_G ratio values for AC, ACH, and ACH-L-Cyst are 0.99, 0.968, and 0.952, respectively. These values suggest that the adsorbents' structures are predominantly composed of amorphous carbon with relatively low levels of structural disorder compared to crystalline solids. The low I_D/I_G ratio of ACH-L-Cyst compared to other AC and ACH adsorbents indicates that incorporating L-cysteine increases the graphitization level of activated carbon, reducing defects and disorder.[36] For the AC-$KMnO_4$ adsorbent, the peak at 635 cm^{-1} corresponds to the symmetric Mn–O stretching vibration in the octahedral MnO_6 structure, providing confirmation of the successful synthesis of the AC-$KMnO_4$ composite. This result also highlights the formation of MnO_2 on the adsorbent surface, reflecting the chemical and structural changes induced by processing. This finding aligns with the results of Kim and Saito (2018), who synthesized a one-pot, purple, benzene-derived MnO_2-carbon hybrid for removing cationic dyes.[37]

3.1.2. SEM images and EDX/EDX-mapping analysis of AC, ACH, ACH-L-Cyst, AC-$KMnO_4$. SEM analysis was performed to examine the surface morphology. The AC, ACH, ACH-L-Cyst, and AC-$KMnO_4$ samples' SEM images are displayed in Fig. 3. The chemical composition of all samples was quantitatively characterized through the use of EDX spectra, and EDX-mapping which are also displayed in Fig. 4.

The morphological characteristics of AC, ACH, ACH-L-Cyst, and AC-$KMnO_4$ were ascertained by SEM analysis; the results are displayed in Fig. 3. Analysis of this figure reveals that AC and ACH adsorbents have a heterogeneous pore distribution with irregular surface characteristics. This heterogeneous pore distribution, consisting of micropores and mesopores, observed in AC and ACH adsorbents is attributed to the thermal decomposition of lignin, cellulose, and hemicellulose during carbonization.[38] EDX analysis of the elemental distribution and EDX-mapping of the AC and ACH materials, as shown in Fig. 4, revealed that they were made up of 2 atoms: carbon and oxygen, not forgetting hydrogen, which cannot appear. SEM analysis of the ACH-L-Cyst adsorbent showed that the pores initially present on the ACH surface had been covered by L-cysteine. ACH-L-Cyst presents a rough, irregular surface after ACH modification, testifying to the successful grafting of organofunctional groups.[9] EDX analysis of element distribution and EDX-mapping images (Fig. 4) show the presence of the elements C, O, N, and S in ACH-L-Cyst. This confirms that the sulfur and nitrogen doping has been successful. The SEM image of the adsorbent AC-$KMnO_4$, obtained by modifying AC with $KMnO_4$, has a more irregular surface with cracks and numerous small particles. This is due to the intensive oxidation of AC by $KMnO_4$, resulting in its degradation and transformation into a brittle, opaque material.[39] The distribution of these small particles on the surface of AC-$KMnO_4$ is rather irregular. It is assumed that these small particles are MnO_2.[3,40] EDX analysis of the elemental distribution and EDX-mapping (Fig. 4) revealed that the AC-$KMnO_4$ surface had been effectively imbued with manganese (Mn), with the presence of carbon and oxygen.

3.1.3. TGA/DTA analysis of AC, ACH, ACH-L-Cyst, AC-$KMnO_4$. The results of the TGA/DTA measurement to analyze the thermal stability and mass loss of the various adsorbents are shown in Fig. 5.

As shown in Fig. 5 above, the curve is divided into three phases: the first extends from 20 °C to 250 °C, the second from 250 °C to 500 °C, 600 °C and the third from 500 °C, 600 °C to 1000 °C. The first weight loss values for AC, ACH, ACH-L-Cyst and AC-$KMnO_4$ are 6.70%, 6.20%, 38.35% and 7.88% respectively, at a temperature of approximately 250–300 °C. This corresponds to the elimination of water content and solvent molecules that were obstructing the material pores from the various adsorbents, indicating that physisorbed water remains in their micropores and mesopores. The highest mass loss value was observed during the second stage, with temperatures ranging from 250–300 °C to 500–600 °C. This result can be explained by the devolatilization of some of the organic matter prior to activation at 500–600 °C,[41] the decomposition of surface chemical groups such as carboxyl and lactonic groups[42] of various adsorbents, and the formation of H_2O, CO, and CO_2 during calcination/activation and synthesis processes.[12] This adsorbent mass loss, which decreases significantly between 250–300 °C and 500–600 °C, is accompanied by a significant exothermic peak at around 555 °C, 587 °C, 473 °C, and 492 °C, respectively for AC, ACH, ACH-L-Cyst, and AC-$KMnO_4$, as illustrated on the DTA curves. This observation could be attributed to carbon oxidation within the adsorbent. Similar reports have been presented by Van and Thi, 2014.[42] Above 500 to 600 °C for the different adsorbents, we observe the third, otherwise negligible, mass loss of 3.86%, 2.85%, 3.46%, and 2.79%, respectively, for AC, ACH, ACH-L-Cyst, and AC-$KMnO_4$. This mass loss is most likely associated with secondary degassing or moisture loss, as well as tar and oxide removal.

3.2. Heavy metal Pb^{2+} adsorption using ACH-L-Cyst and AC-$KMnO_4$

3.2.1. Impact of AC, ACH, ACH-L-Cyst, and AC-$KMnO_4$ modifications on Pb^{2+} adsorption. The current work examines the effects of altering AC, ACH, ACH-L-Cyst, and AC-$KMnO_4$ on Pb^{2+} adsorption at 210 mg L^{-1} during stirring for 240 minutes. To choose the top-performing adsorbents, this work was done before the optimization stage. As shown in Fig. 6, the maximum adsorption percentage of ACH-L-Cyst and AC-$KMnO_4$ is significantly greater than that of AC and ACH.

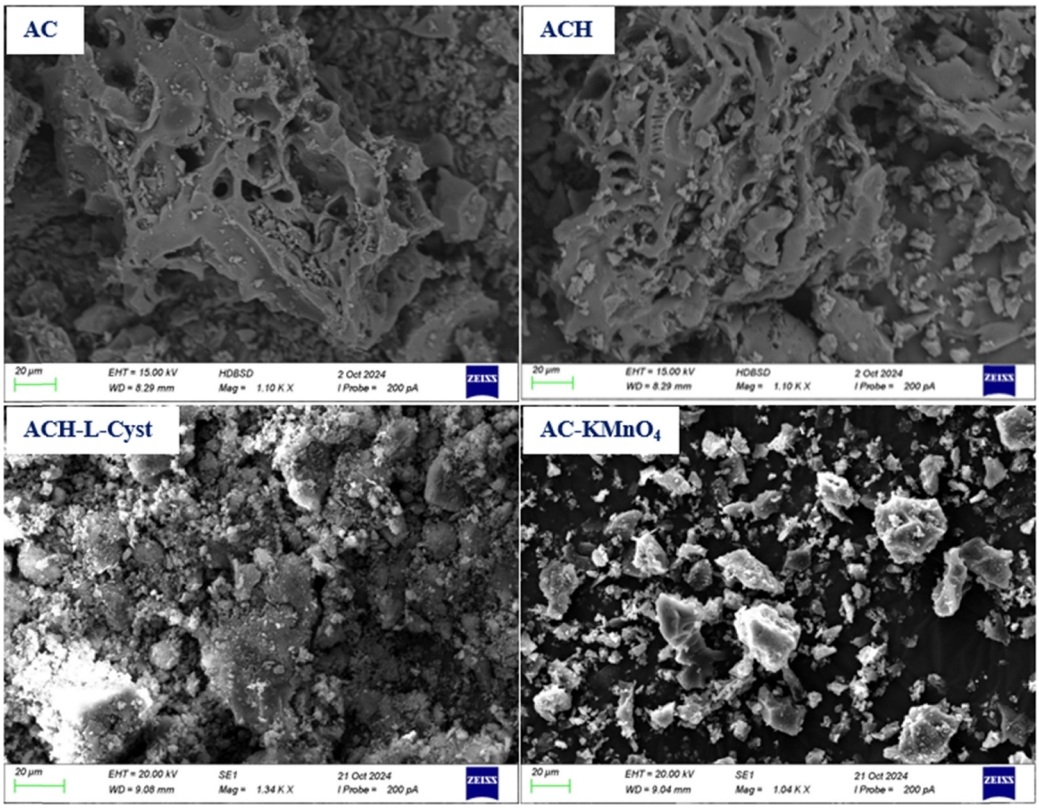

Fig. 3 SEM images of AC, ACH, ACH-L-Cyst, AC-$KMnO_4$.

The new material functionalities, in particular the –SH and $–NH_2$ functions in ACH-L-Cyst and the Mn–O function in AC-$KMnO_4$, explain the significantly higher adsorption percentage observed for these two doped materials compared with undoped AC and ACH materials. This observation highlights particularly strong interaction forces between the solute and the surface of the two adsorbents ACH-L-Cyst, and AC-$KMnO_4$.[43] For the adsorbents AC, ACH, ACH-L-Cyst, and AC-$KMnO_4$, respectively, the percentages of Pb metal ion adsorption are 57.42%, 66.14%, 85.20%, and 98.47%. Clearly, this modification has increased the amount of Pb^{2+} ions that can be adsorbed. According to our study, the maximum adsorption percentage of Pb by AC-MnO_4 is significantly higher than that of ACH-L-Cyst, AC, and ACH, which favored the creation of MnO_2 and improved the properties of the AC-MnO_4 adsorbent. However, Pb removal by AC-MnO_4 could be mainly controlled by cation exchange. In addition, a considerable release of Mn into the equilibrium solution could occur, following the formation of an inner-sphere complex between Pb and MnO_2 and their exchange with Mn.[26,44] N- and S-doped ACH-L-Cyst adsorbent shows superior adsorption performance to AC and ACH for Pb^{2+} removal. This finding can be attributed to exchange of electrons between the functional groups present on the surface of ACH-L-Cyst and Pb^{2+} ions during the adsorption process, once the adsorbent pores have reached saturation. This can also be explained by the fact that the amino and sulfide groups are free and available for adsorption. Similar results have been presented by Zhu *et al.* 2022.[9] For the continuation of our research, we have opted to use ACH-L-Cyst and AC-$KMnO_4$ adsorbents, in line with previous results.

3.2.2. Optimization of Pb^{2+} adsorption by ACH-L-Cyst and AC-$KMnO_4$

– Analysis of variance

Using the CCD model, the analysis of variance (ANOVA) was utilized to assess the simultaneous and individual effects of factors involved in the adsorption of Pb^{2+} ions on ACH-L-Cyst and AC-$KMnO_4$. The factors taken into account have a significant impact on the effectiveness of elimination. The CCD-optimized model for Pb^{2+} elimination proposed a quadratic model with adjusted R^2 and predicted R^2 values close to one, as shown in Tables S5 and S6. High R^2 values indicate that the model fits the dataset well, confirming the validity of the proposed model.[45] Results, including linear, cross and quadratic terms for all factors, are presented in Table 2.

Analysis of the table indicates that the ACH-L-Cyst model is highly significant (F = 31.75; $p < 0.0001$), with a 0.01% probability that this value is due to experimental noise. Terms A, B, C, D, as well as interactions AB, AC, AD, BC, BD, and quadratic terms A^2, B^2, C^2, and D^2 are significant ($p < 0.05$). Similarly, the AC-$KMnO_4$ model is highly significant (F = 59.69; $p < 0.0001$). Factors A, B, C, interactions AB, AC, AD, BC, BD, CD, and quadratic terms A^2, B^2, C^2, and D^2 contribute significantly to the model ($p < 0.05$). For ACH-L-Cyst and AC-$KMnO_4$ 13 effects have p-values below 0.05, indicating that they are

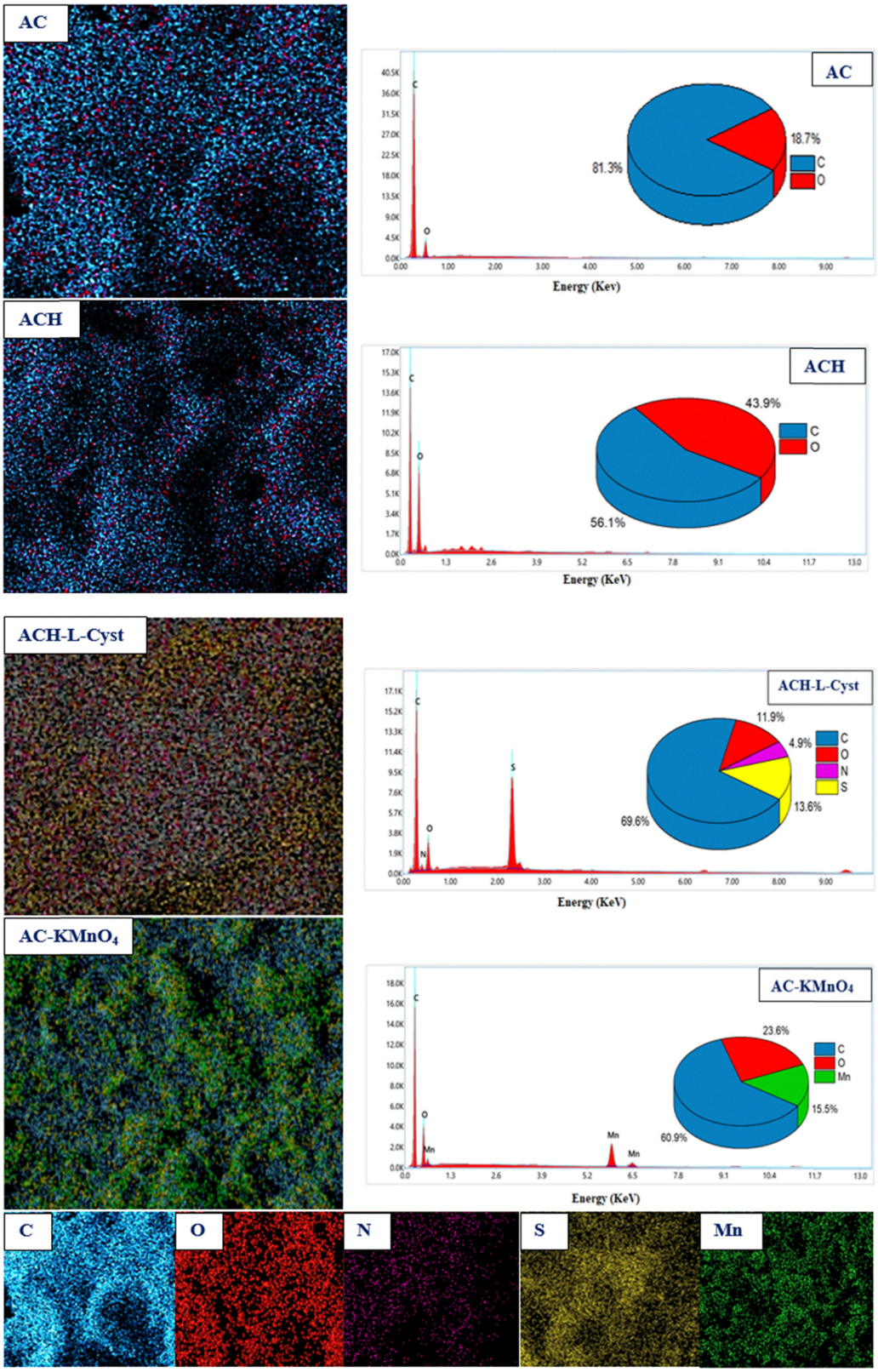

Fig. 4 EDX/EDX-mapping analysis of AC, ACH, ACH-L-Cyst and AC-$KMnO_4$.

significantly different from zero at the 95.0% confidence level. Similar results have been presented by Fotsop *et al.* 2025.[46] However, pH, Pb^{2+} ions concentration, and stirring time showed significant effects both linearly and crosswise for adsorbed Pb^{2+} ions. This indicates that, when combined together, the model is statistically significant at the 95.0%

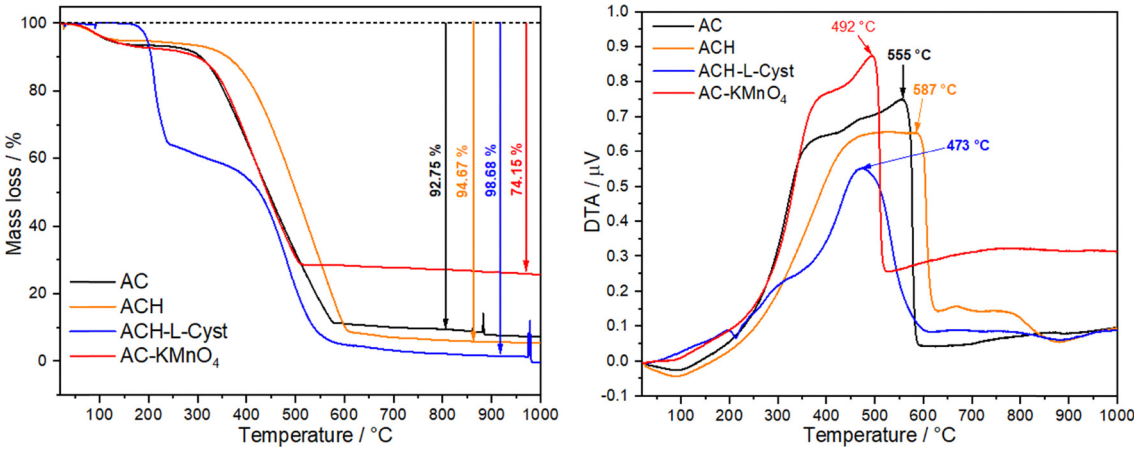

Fig. 5 TGA/DTA plot of AC, ACH, ACH-L-Cyst and AC-$KMnO_4$.

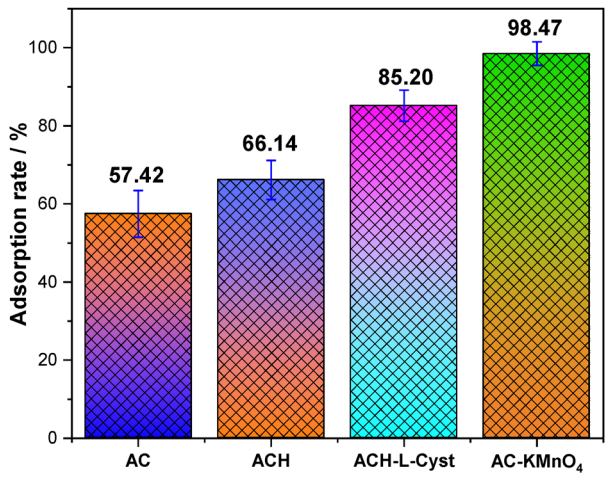

Fig. 6 Comparison of maximum percentage adsorption at a high initial concentration of 210 mg L^{-1} for AC, ACH, ACH-L-Cyst, and AC-$KMnO_4$, dosage of adsorbent 70 mg, time 240 min.

confidence level for both the crossover and quadratic terms of all four factors. The Pareto diagram (Fig. 7a and b) and normal adsorption probability diagram (Fig. S1a and b) show the positive effect of pH compared to mass, stirring time and concentration, which show a negative effect for ACH-L-Cyst, meaning that the increase in the percentage adsorption of Pb^{2+} ions is strongly influenced by the pH of the medium. For AC-$KMnO_4$, we observe the positive effect of time and mass compared to concentration and pH, which show a negative effect, meaning that the increase in adsorption percentage is strongly influenced by adsorption kinetics.

- The adsorption experiments' experimental design

The adsorption percentages, coded experimental matrix, observed and predicted values are presented in Table 3. P1 and P2 represent the percentages of Pb^{2+} ions adsorbed on ACH-L-Cyst and AC-$KMnO_4$ respectively. Eqn (5) and (6) represent the quadratic model illustrating the relationship between the percentage of Pb^{2+} ions adsorbed, considered as a response, and the independent variables: pH (A), time (B), concentration (C) and mass (D). Positive values indicate a synergistic effect between the variables, while negative values reveal an antagonistic effect. Residual values, corresponding to the difference between observed and predicted values, are presented in Table S7.

$$P1 = 55.6778 - 5.62054A - 0.510509B - 0.325367C + 2.86258D + 0.694188A^2 + 0.0197062AB + 0.0088968AC - 0.0432291AD + 0.00121636B^2 + 0.000247078BC + 0.000604596BD + 0.000546713C^2 + 0.000143247CD - 0.0234121D^2 \quad (5)$$

$$P2 = 75.1024 + 14.2129A - 0.222977B + 0.0432102C - 0.226996D - 1.27396A^2 + 0.014416AB - 0.00640524AC - 0.0388141AD + 0.000397921B^2 + 0.000146501BC + 0.000655029BD - 0.000112754C^2 - 0.000302579CD + 0.00342447D^2 \quad (6)$$

The goodness-of-fit of the regression model was assessed by means of the R^2, adjusted R^2, standard error of estimation and mean absolute error. For P1, the R^2 and adjusted R^2 values are 97.16% and 94.10% respectively, while for P2 they are 98.47% and 96.82% respectively. The close similarity between R^2 and adjusted R^2 indicates a strong correlation between the factors studied and the accuracy of the central composite design adopted.[47] For P1, the standard error of the estimate indicates that the standard deviation of the residuals is 4.35615. The mean absolute error (MAE) of 2.29756 corresponds to the mean value of the residuals. For P2, the standard error of the estimate shows that the standard deviation of the residuals is 1.84691. The mean absolute error (MAE) of 1.0415 corresponds to the mean value of the residuals. Taken together, these results show that the model's noise-to-ratio values are within the desirable range.[1] The accuracy of the regression model was assessed by means of parity and residual plots, as shown in Fig. 8. Fig. S2

Table 2 *F*-Value and *p*-value of the analysis of variance (ANOVA) for the adsorption of Pb^{2+} ions on ACH-L-Cyst and AC-$KMnO_4$

		ACH-L-Cyst		AC-$KMnO_4$	
	Factors	*F*-Value	*p*-Value	*F*-Value	*p*-Value
Model		31.75	<0.0001	59.69	<0.0001
Linear term	A-pH	77.34	<0.0001	8.97	0.0103
	B-Time	8.72	0.0112	20.22	0.0006
	C-Concentration	5.27	0.0390	252.14	<0.0001
	D-Mass	5.26	0.0391	0.3644	0.5565
Cross term	AB	40.69	<0.0001	121.13	<0.0001
	AC	21.68	0.0004	62.52	<0.0001
	AD	22.69	0.0004	101.76	<0.0001
	BC	25.65	0.0002	50.18	<0.0001
	BD	6.81	0.0216	44.46	<0.0001
	CD	0.9993	0.3357	24.80	0.0003
Quadratic term	A^2	5.31	0.0384	99.41	<0.0001
	B^2	38.33	<0.0001	22.82	0.0004
	C^2	52.95	<0.0001	12.53	0.0036
	D^2	190.74	<0.0001	22.70	0.0004

*p-Value significant ($p < 0.05$).

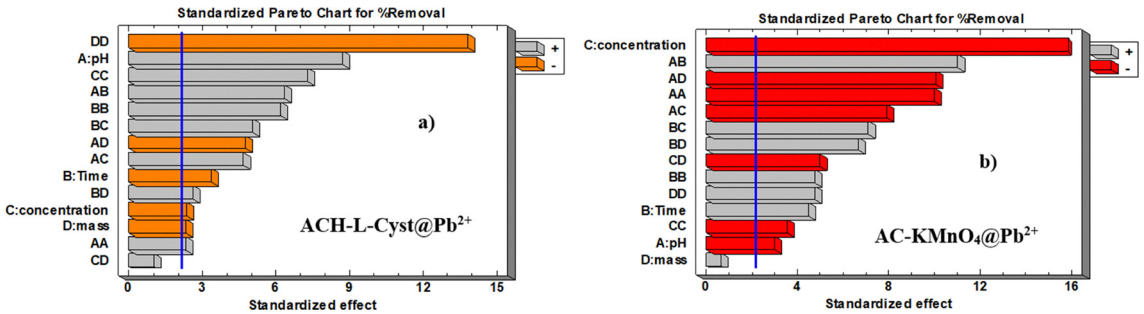

Fig. 7 Pareto diagrams of the effects of factors A, B, C and D for Pb^{2+} adsorption onto ACH-L-Cyst (a) and AC-$KMnO_4$ (b).

illustrates the relationship between externally examined residuals and Pb^{2+} ions adsorption, together with the corresponding normalized residual plot.

Fig. 8a and c shows that the maximum data points lie almost on the straight line that predicts the observed and predicted values of Pb^{2+} ions and that they are almost identical, testifying to the predictive effectiveness of the regression model.[1,7] Fig. 8b and d shows that the residuals are randomly dispersed, without any regularity that might justify fitting the experimental data. It can also be seen that the maximum deviation between predicted and observed values of Pb^{2+} ion removal is less than 4%, indicating a good correlation between the two. Fig. S2a & c shows a normal residual plot with a normal distribution for Pb^{2+} ion adsorption. The residual plots show almost linear behavior, indicating that the model prediction is accurate. Similar results were obtained by Zaman *et al.*,[7] and Birniwa *et al.*[48] in 2022. Fig. S2b & d illustrates the correlation between externally analyzed residuals and Pb^{2+} ion removal. It highlights a strong correlation between the variables. Birniwa *et al.* obtained similar results in 2022.[48]

– Exploration of interaction factors related to Pb^{2+} ion adsorption and model confirmation

The 3D evaluation of the response surface of the variables pH (A), time (B), concentration (C) and mass (D) that interact synergistically to optimize the uptake of Pb^{2+} ions by the two adsorbents are displayed in Fig. 9 and Fig. S3. The 2D surface plot of different variable are show in Fig. S4 and S5. The percentage adsorption of Pb^{2+} ions was influenced by these different process variables. These figures show how ACH-L-Cyst and AC-$KMnO_4$, respectively, interact and depend on pH, contact time, concentration, and adsorbent mass to remove a certain percentage of Pb^{2+} ions in aqueous solution. The results indicate that the removal percentage rises with increasing pH of solution, from 2 to 5. Above pH 5, increasing the pH of the metal solution decreases the percentage of adsorption, depending on time and leads concentration (Fig. 9a-1, a-2; b-1 and b-2). This is explained by the competition to occupy the adsorption sites between the metal ions and the hydroxyl ions, modifying the surface charge and causing electrostatic repulsion between the adsorbent and the metal ions, which leads to the leakage of the adsorbed ions. In addition, the combined impact of the initial concentration of Pb^{2+} ions and pH was assessed (Fig. 9a-2; b-2 and Fig. S3). This shows adsorption of 80% of Pb^{2+} ions for ACH-L-Cyst and 85% for AC-$KMnO_4$, from an initial Pb^{2+}

Table 3 Observed and predicted values from the adsorption of Pb^{2+} ions using the central composite design

Run order	pH	Time (min)	Concentration (mg L^{-1})	Mass (mg)	P1: % Pb^{2+} removed by ACH-L-Cyst		P2: % Pb^{2+} removed by AC-$KMnO_4$	
					Observed value	Predicted value	Observed value	Predicted value
1	+1	−1	−1	+1	70.31	66.71	88.65	86.77
2	0	0	0	0	61.77	64.95	90.30	91.02
3	0	0	0	0	65.33	64.95	90.34	91.02
4	−1	+1	+1	+1	55.54	56.11	90.11	90.34
5	0	+1	0	0	80.35	78.71	98.68	98.47
6	0	−1	0	0	84.20	84.77	95.33	94.55
7	+1	+1	+1	+1	93.53	87.83	80.60	81.28
8	−1	1	−1	−1	50.02	48.58	73.90	74.32
9	0	0	0	−1	30.14	29.84	95.26	96.23
10	0	0	−1	0	85.76	87.04	94.70	93.86
11	−1	0	0	0	62.39	62.16	80.02	80.85
12	0	0	0	0	65.51	64.95	90.03	91.02
13	−1	−1	−1	+1	86.06	83.06	98.44	101.55
14	−1	+1	−1	+1	58.55	57.75	96.78	94.92
15	+1	+1	+1	−1	90.52	95.05	90.13	88.51
16	+1	−1	+1	+1	60.31	63.28	53.43	54.50
17	−1	+1	+1	−1	40.25	42.58	78.31	78.94
18	0	0	0	+1	25.91	25.13	98.72	96.76
19	0	0	0	0	63.96	64.95	90.42	91.02
20	+1	−1	+1	−1	82.35	81.88	73.44	74.05
21	+1	0	0	0	81.07	80.22	80.07	78.25
22	+1	+1	−1	−1	85.50	80.77	98.57	98.50
23	−1	−1	+1	−1	62.53	57.19	85.09	84.81
24	+1	−1	−1	−1	88.68	89.65	95.86	97.12
25	−1	−1	+1	+1	55.89	59.35	85.06	83.89
26	+1	+1	−1	1	62.31	69.19	98.68	100.46
27	0	0	+1	0	84.68	82.33	80.18	80.03
28	−1	−1	−1	−1	80.82	85.26	95.20	93.27

ions concentration of 400 mg L^{-1}, during 122 minutes of agitation, at pH 8. The impacts of the concentration of Pb^{2+} ions and contact time on the sorption performance of Pb^{2+} ions are shown in Fig. 9a-3 and b-3. Pb^{2+} ion removal efficiency decreases as contact time and Pb^{2+} ions concentration increase. Fig. 9a-4 and b-4 illustrate how contact time and mass affect Pb^{2+} ions sorption. The percentage of Pb^{2+} ions sorption decreased with increasing contact time. This is because over time, more Pb^{2+} ions were adsorbed onto the surface of both adsorbents, reducing the contact area and available sorption sites. However, after 122 minutes, maximum adsorption is reached with both adsorbents. The adsorption percentage is higher at the beginning of the stirring time, because a large number of free adsorption bonding sites are available.[1] Optimum conditions for the factors studied for the adsorption of Pb^{2+} ions predicted by the Design-Expert 13 software are displayed in Table S8. Predicted values are close to those obtained experimentally for the percentage of Pb^{2+} removed under these optimal conditions. The close agreement between the predicted and optimal experimental values corroborates the high R^2 and adjusted R^2 values presented in Tables S5 and S6 for the empirical models of Pb^{2+} ion adsorption by the two adsorbents and suggests that the models employed to represent Pb^{2+} ion adsorption by ACH-L-Cyst and AC-$KMnO_4$ are valid. Fig. 9a-5 and b-5 show the factors' perturbation graph. Fig. 9a-6 and b-6 show the percentage adsorption at each factor point.

In numerical optimization, the program aims to optimize the objective function in order to determine the optimal conditions.[11,49] The maximum adsorption capacity of Pb^{2+} ions on ACH-L-Cyst and AC-$KMnO_4$, as well as the corresponding optimal experimental conditions, were determined using the desirability function (Fig. 10). We applied a multi-response method to optimize combinations of four factors: pH (2–8), time (2–240 min), initial Pb^{2+} ion concentration (20–400 mg L^{-1}), and adsorbent mass (20–100 mg). Our goal was to identify conditions that would produce an optimal response of 100%. The optimal conditions were found to be a pH of 5.0, a time of 122.5 min, a Pb^{2+} ion concentration of 210 mg L^{-1}, and an adsorbent mass of 60 mg, resulting in maximum removal efficiencies of 78.82% for ACH-L-Cyst and 98.85% for AC-$KMnO_4$, respectively with the desirability value of 1.00. Optimal predicted conditions were verified experimentally, and the results are presented in Table S8. Consequently, this model can be used to optimize the removal of Pb^{2+} ions and predict the percentage of lead removed.[50]

3.2.3. Modelling of adsorption kinetics. Pb^{2+} adsorption kinetics under optimum conditions are shown in Fig. 11(a–c) respectively. The results show a high adsorption capacity for the AC-$KMnO_4$ adsorbent compared with the ACH-L-Cyst adsorbent. Fig. 11a shows that for both adsorbents, the adsorption of Pb^{2+} ions grows rapidly at first, then decreases and finally stabilizes when equilibrium is reached after pore saturation, as shown by the plateau obtained after 120 minutes with a significantly high adsorption capacity of 67.676 mg g^{-1} for ACH-L-Cyst and 86.274 mg g^{-1} for AC-$KMnO_4$. The efficient complexation of organic groups on both adsorbents' surfaces with Pb^{2+} is responsible for the quick rise in adsorption capacity[9,51,52] as well as electrostatic attraction or oxydation

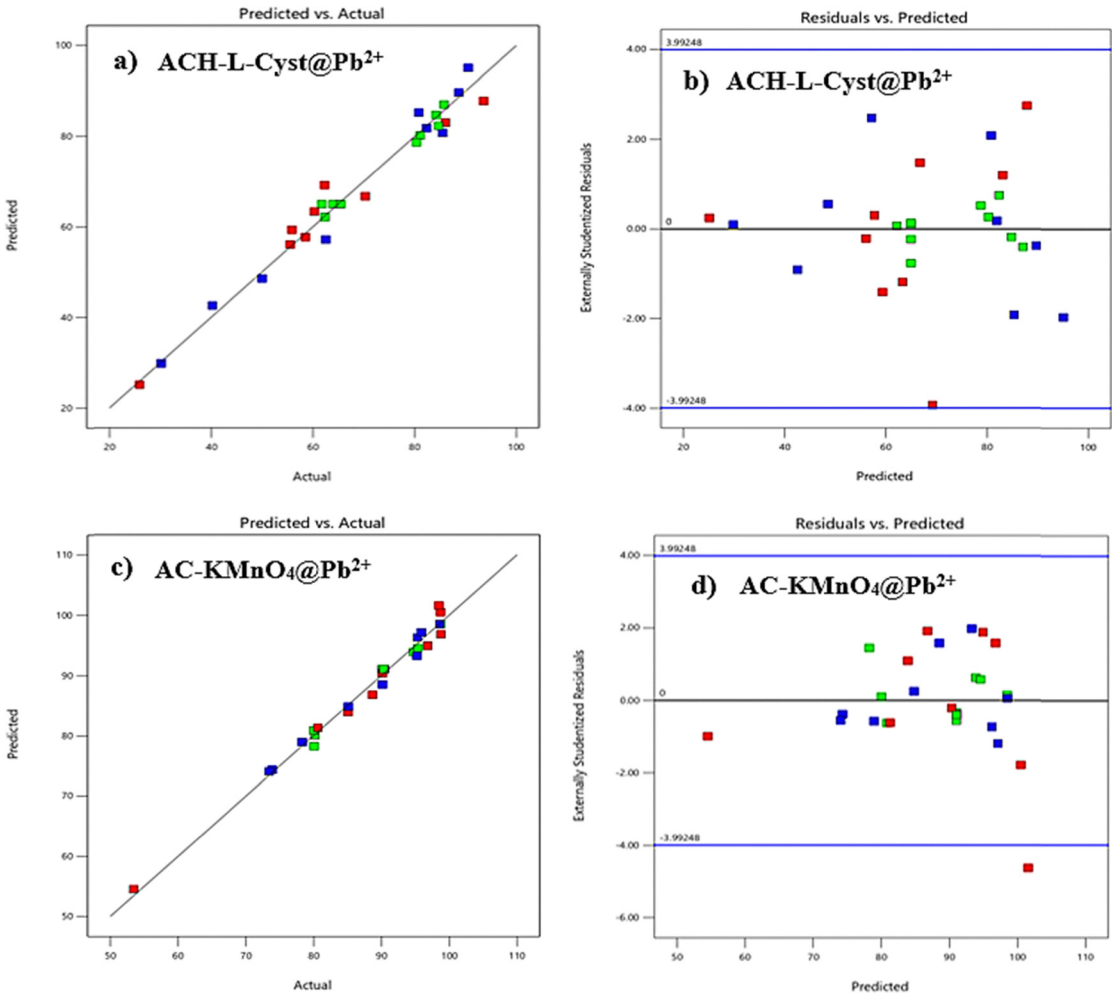

Fig. 8 (a and c) Correlation between predicted *vs.* observed values of the Pb^{2+} removal efficiency and (b and d) plot between residuals and predicted values.

and precipitation. The plateau observed after 120 minutes could be attributed to a decreasing number of available contact sites and intense repulsive forces between Pb^{2+} ions.[53] The kinetic models PFO, PSO, intra-particle diffusion, and Elovich[54] presented in Table S2 were used to fit the experimental data in order to examine the Pb^{2+} adsorption behavior on both adsorbents. Fig. 11(b and c), displays the fitting curves, and Table 4 presents the non-linear fitting parameters that were found. This table shows that the sorption mechanism of Pb^{2+} ions on both adsorbents is best described by the PFO, PSO and Elovich kinetic models, due to the R^2 value > 0.99 and which are relatively close. However, Elovich's model yields an $R^2 > 0.99$ with an α value of 10^{22} mg g^{-1} min^{-1}, which is extreme and physically unrealistic. This implies an initial adsorption rate exceeding the limits of molecular diffusion. This phenomenon can be explained by a numerical artifact during nonlinear regression, due to the strong correlation between α and β. Thus, even though the Elovich model provides a satisfactory empirical fit of the kinetic data, its parameters do not allow for an interpretation of the adsorption mechanisms. Thus, we can say that, in the medium, there is a coexistence of physical adsorption such as ion exchange, electrostatic interaction, or hydrogen bonding and chemical adsorption such as electron transfer or complexation during the removal of Pb^{2+} from the solution. This result also highlights the heterogeneous adsorbent surface. In addition, the Q_{ads} values determined by the pseudo-first and pseudo-second order models are closer to those obtained from the tests (Table 4). However, the pseudo-first order model best explains the Pb^{2+} adsorption kinetics given the low values of χ^2, RMSE, ARE, and SCE observed in Table 4. This reveals a van der Waals-type interaction between Pb^{2+} ions and the ACH-L-Cyst and AC-$KMnO_4$ adsorbents and indicates that multilayer adsorption dominates at the surface of the adsorbents. Zbair *et al.* 2019[55] and El-Rayyes *et al.* 2025[56] have reported similar results.

3.2.4. Modelling of adsorption isotherms. Adsorption isotherms of Pb^{2+} ions by ACH-L-Cyst and AC-$KMnO_4$ adsorbents under optimal conditions are shown in Fig. S6. Different isotherm models such as Langmuir, Freundlich, Jovanovic, Temkin, Dubinin–Raduskevish, Langmuir–Freundlich, and Redlich–Peterson were used to fit the experimental adsorption curves concerning the removal of Pb^{2+} ions. The aim was to

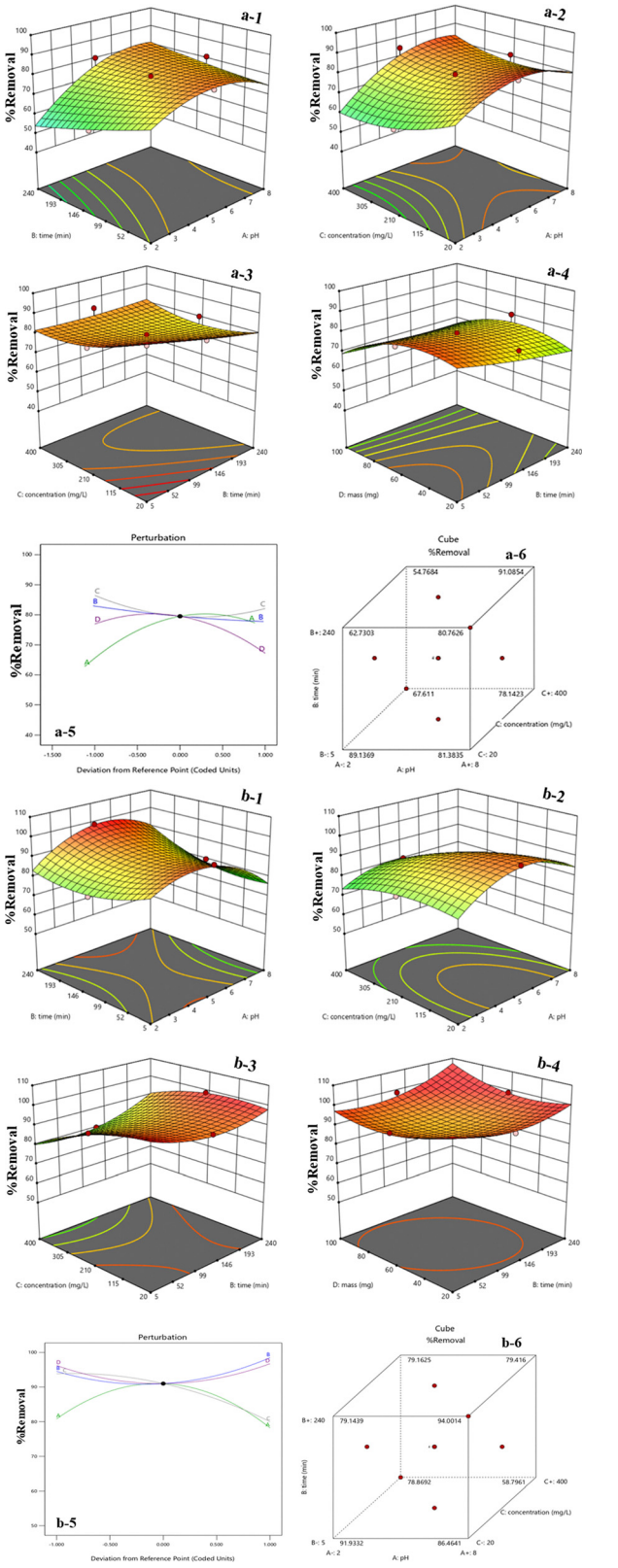

Fig. 9 CCD response surface graphs in 3D illustrating the impact of pH, time (min), concentration of Pb^{2+} (mg L^{-1}) and mass (mg) on the adsorption of Pb^{2+} ions (%removal) using ACH-L-Cyst (a-1 to a-4) and AC-$KMnO_4$ (b-1 to b-4), respectively; perturbation graph (a-5 & b-5) and %removal at each factorial point (a-6 & b-6).

determine the favorable adsorption mechanism. Fig. 12(a–c) show the corresponding curves and Langmuir separation factor, respectively. The AC-$KMnO_4$ adsorbent has a greater capacity to remove Pb^{2+} ions compared to the ACH-L-Cyst adsorbent. For example, the equilibrium adsorption quantities were 86.1 mg g^{-1} and 68 mg g^{-1} for the adsorbents AC-$KMnO_4$ and ACH-L-Cyst, respectively. Effective removal was 98.47% for AC-$KMnO_4$ and 77.20% for ACH-L-Cyst, respectively. Fig. S6 shows that the higher the concentration of Pb^{2+} ions, the greater the quantity adsorbed per gram of adsorbent. The explanation for this phenomena is that, when initial Pb^{2+} ion concentrations are low, the number of Pb^{2+} ions present in the aqueous solution is less than the available active sites on the surface of each adsorbent,[57] thereby increasing adsorption rate. The increase in adsorption capacity, which is linked to the rise in the initial concentration of Pb^{2+} ions, can be elucidated by the fact that the higher the concentration, the greater the number of ions in solution and the more active sites on the adsorbent surface are covered.[57,58] We can also say that increasing the initial concentrations of Pb^{2+} ions created stronger interactions between the Pb^{2+} ions in solution and the surface of each adsorbent.[59] This can also be explained by the significant mass transfer driving force at high concentrations of lead.[8] For all the isotherm models studied, the parameters calculated using their non-linear forms are reported in Table 5. This table shows that $R^2 > 0.95$ for all models is very good for both adsorbents, with the exception of the Dubinin-Radushkevich model for the ACH-L-Cyst adsorbent. Adsorption isotherm data are best described by the non-linear models Langmuir–Freundlich, Langmuir, Temkin, Redlich–Peterson, Freundlich, and Jovanovic for ACH-L-Cyst and Langmuir–Freundlich, Redlich–Peterson, Temkin, Jovanovic, Langmuir, and Freundlich for AC-$KMnO_4$. The Langmuir–Freundlich model indicates that the adsorption energy is distributed between the different surfaces and the adsorption surface is heterogeneous.[60] It is assumed that interactions between the adsorbate and the adsorbent would also lead to adsorption provided that the adsorption surface is homogeneous.[60] With regard to the Redlich–Peterson model, we can say that the adsorption of Pb^{2+} ions by both adsorbents occurs on heterogeneous surfaces. The MLF and g values obtained using the Langmuir–Freundlich and Redlich–Peterson isotherm models differ from 1. This indicates that the two adsorbents' adsorption of Pb^{2+} ions can't be simplified to the Langmuir isotherm.[61,62] The high R^2 values obtained demonstrate the relevance of all these models for the Pb^{2+} ions adsorption in aqueous solution. Thus, these models are associated with the adsorption of materials with a heterogeneous surface.[61,62] Concerning the Langmuir isotherm, we can state that the adsorption of Pb^{2+} ions by both adsorbents corresponds to monolayer sorption, with identical adsorption sites finite on a homogeneous surface.[14,63] The low K_L value shows that Pb^{2+} ions and the adsorbents ACH-L-Cyst and AC-$KMnO_4$ have a strong interaction. Langmuir isotherm separation factor values between 0 and 1 (Fig. 12c) suggest that Pb^{2+} ions are favorably adsorbed by both adsorbents. Based on the Freundlich model, we can conclude that there is also multilayer

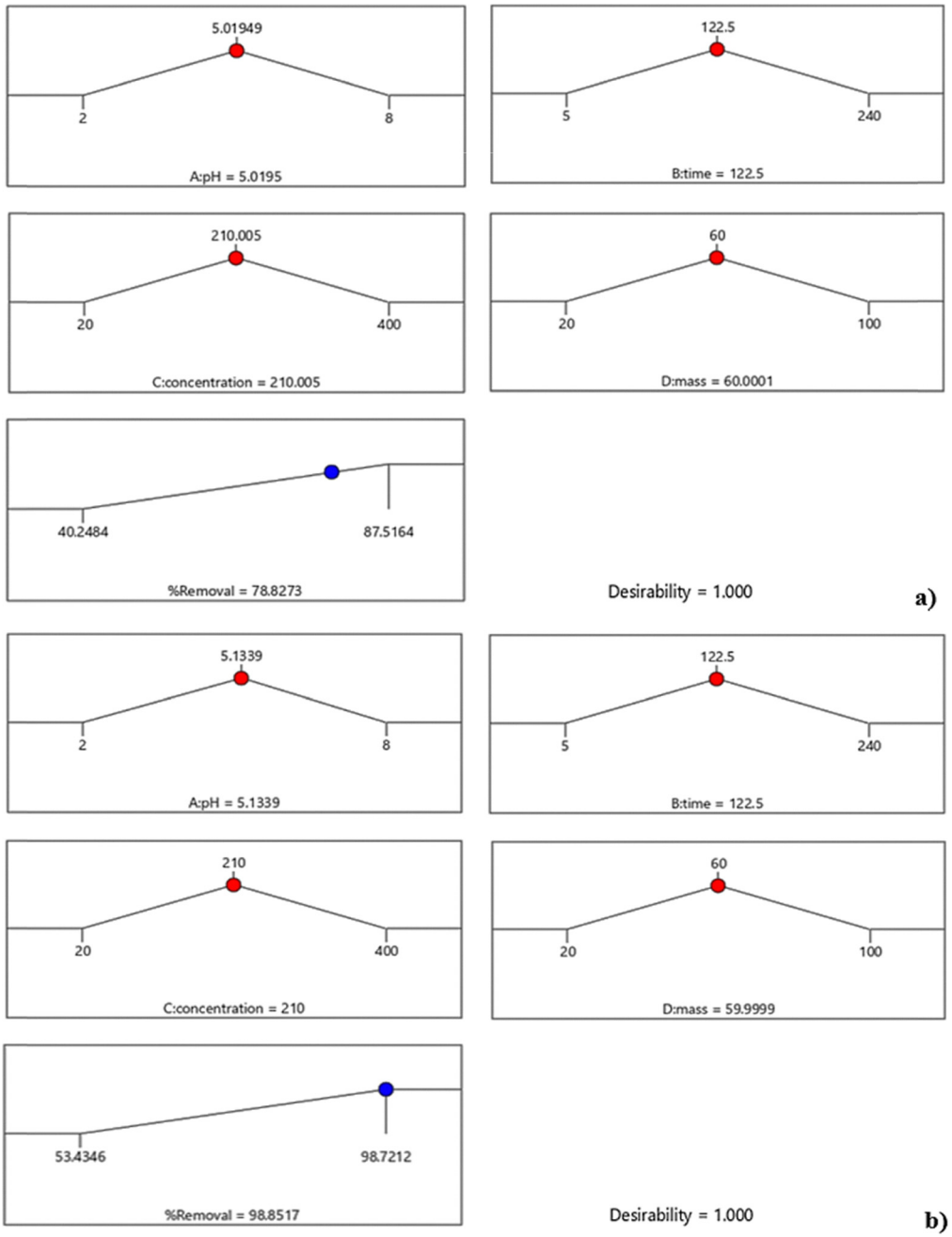

Fig. 10 Desirability ramp for the numerical optimization of four factors, such as pH, time, concentration, and adsorbent mass using ACH-L-Cyst (a) and AC-$KMnO_4$ (b).

adsorption on a heterogeneous surface for both adsorbents and that interactions between the adsorbate and the adsorbent surface are an important factor in the adsorption process.[63,64] The Freundlich model's $1/n$ values are less than 1, indicating a strong affinity between the adsorbents' surface and the adsorbed Pb^{2+} ion solution. This also suggests that the adsorption sites are more heterogeneous and that adsorption is due to a physical process. The Temkin isotherm indicates that an electrostatic interaction may exist between the two adsorbents and the Pb^{2+} ions. This indicates that the adsorption energy of the surface reduces linearly when the active sites are invaded by Pb^{2+} ions.[8] According to Temkin's model, the adsorption process is exothermic since the change in adsorption energy ΔQ is positive, regardless of the material considered. Jovanovic's model, for its part, indicates that during the sorption of Pb^{2+} ions by the two adsorbents, it is likely that a localized non-ideal monolayer will form without lateral interaction. Among the isotherms selected in Table 5, for which we have presented the information that each can provide to describe the adsorption process, the Langmuir–Freundlich isotherm stands out for its ability to best describe the adsorption process. Indeed, it has the highest R^2 and the lowest χ^2, RMSE, ARE and SCE error

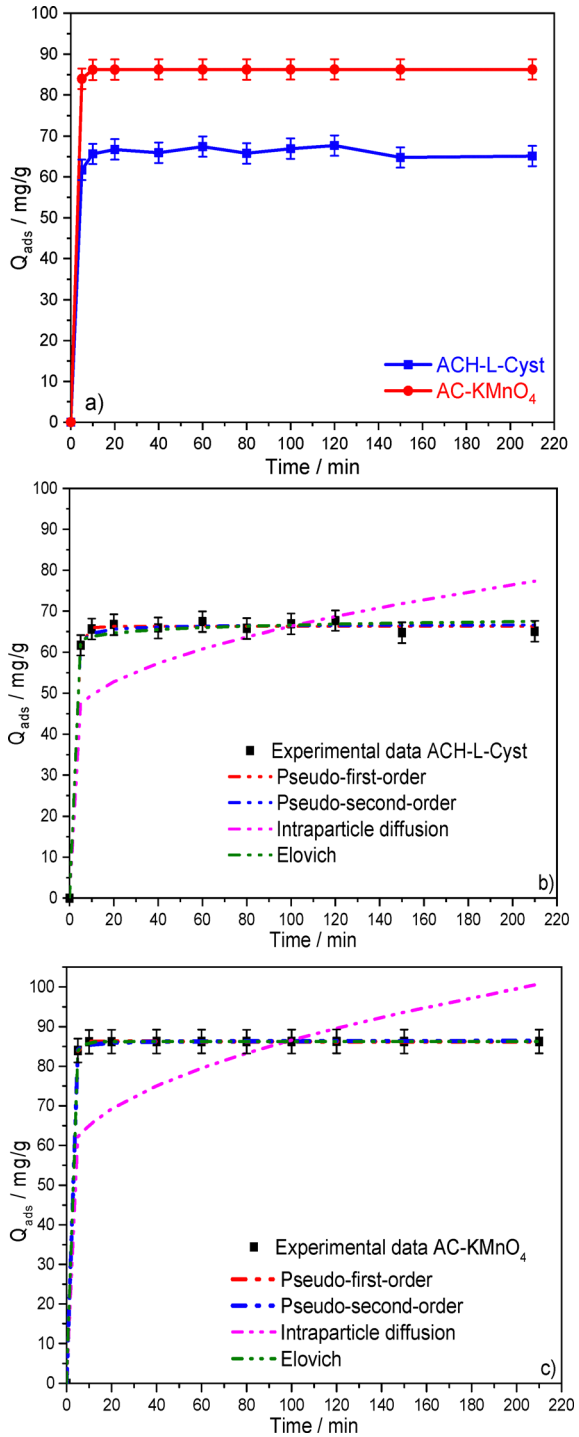

Fig. 11 Time effects of Pb^{2+} adsorption (a) and non-linear kinetics studies (b and c).

functions, regardless of the adsorbent.[65] The maximum adsorption capacities determined using the Langmuir–Freundlich isotherm are 113 mg g^{-1} and 141 mg g^{-1} for ACH-L-Cyst and AC-$KMnO_4$, respectively.

3.2.5. Thermodynamic study of adsorption. The following thermodynamic characteristics were assessed in order to ascertain if the adsorption process is endothermic or exothermic: enthalpy change (ΔH°), standard free energy (ΔG°) and entropy change (ΔS°). The following formulas are used to compute these thermodynamic characteristics of adsorption processes:

$$\Delta G^\circ = \Delta H^\circ - T\Delta S^\circ = -RT\ln K_D \quad (7)$$

$$\ln K_D = \frac{-\Delta H^\circ}{RT} + \frac{\Delta S^\circ}{R} = -\frac{\Delta G^\circ}{RT} \quad (8)$$

$$K_D = \frac{Q_e}{C_e} \quad (9)$$

where K_D is the distribution coefficient for adsorption, R is the gas constant (8.314 J mol^{-1} K^{-1}), T is absolute temperature (K), Q_e is the amount of Pb^{2+} ions (mg g^{-1}) that are adsorbed on the adsorbent at equilibrium, C_e is the Pb^{2+} ion's equilibrium concentration in the solution (mg L^{-1}). Plot of $\ln K_D = f(1/T)$ and adsorption efficiency *versus* temperature is showed in Fig. 13. Calculating the *y*-intercept and slope of the graphs allowed us to get the values of ΔS° and ΔH°.

By increasing the solution temperature from 298 K, 308 K and 318 K, Pb^{2+} ion removal percentages also increase (Fig. 13a). However, this increase is not very significant when the temperature rises, showing the adsorbent's effectiveness even at low temperatures.[66] Higher temperatures increase the mobility of Pb^{2+} ions and decrease the viscosity of the solution, promoting a more significant interaction between these ions and the surface of each adsorbent.[56] The values of the thermodynamic parameters for Pb^{2+} adsorption are shown in Table 6.

According to this table, $\Delta G^\circ < 0$ and decreases further with increase in temperature, suggesting spontaneous adsorption process of Pb^{2+} by ACH-L-Cyst and AC-$KMnO_4$ and that spontaneity rises with temperature. These negative values of ΔG° also show that the adsorption process is thermodynamically possible.[67] Pb^{2+} ion adsorption is an endothermic process, as demonstrated by the positive value of ΔH°. ΔH° values < 20 kJ mol^{-1}, show that the adsorption interactions that occur are physical in nature. Values of $\Delta S^\circ > 0$ suggest an aleatory nature at the solution–solid interface during adsorption.[66,68]

3.2.6. Selective adsorption of Pb^{2+} ions towards different cations. In order to verify the selectivity of ACH-L-Cyst and AC-$KMnO_4$ with respect to Pb^{2+}, several other metals were mixed in the same solution with the latter. This study offers an analogy with reality, as it is difficult to observe a single type of ion in the real medium. The adsorption results for the different metals by ACH-L-Cyst and AC-$KMnO_4$ are shown in Fig. 14a. It is clear that Pb^{2+} ion selective adsorption is effective. Indeed, the high adsorption percentage, equivalent to 97.064% for AC-$KMnO_4$ and 76% for ACH-L-Cyst when the ions are mixed, is very close to the adsorption rate when lead(II) ion is alone in solution. This slight difference can be explained by competition between ions to occupy the active sites of the adsorbent, although it is insignificant or negligible. It is therefore clear that ACH-L-Cyst and AC-$KMnO_4$ have a strong affinity for Pb^{2+} ions, thereby limiting the availability of adsorption sites for other competitors. This affinity could be explained by the fact that the Pb of the Lewis acid and the –SH–, –NH–, and –OH groups of the

Table 4 Parameters of kinetic models

Models	Parameters	Values	R^2	χ^2	RMSE	ARE	SCE
ACH-L-Cyst							
Pseudo-first order	Q_{ads} (mg g^{-1})	66.263	0.998	0.121	0.999	1.134	7.989
	K_1 (min^{-1})	0.534					
Pseudo-second order	Q_{ads} (mg g^{-1})	66.679	0.997	0.176	1.207	1.505	11.663
	K_2 (g mg^{-1} min^{-1})	0.046					
	h (mg g^{-1} min^{-1})	204.974					
	$t_{1/2}$ (min)	21.691					
Intraparticle diffusion	C (mg g^{-1})	41.8617	0.497	17.942	11.068	12.653	980.017
	K_{id} (mg g^{-1} min$^{-0.5}$)	2.4479					
Elovich	α (mg g^{-1} min^{-1})	2.27×10^{22}	0.994	0.355	1.710	2.048	23.406
	β (g mg^{-1})	0.839					
AC-$KMnO_4$							
Pseudo-first order	Q_{ads} (mg g^{-1})	86.248	0.999	2.11729×10^{-4}	0.015	0.012	0.002
	K_1 (min^{-1})	0.7267					
Pseudo-second order	Q_{ads} (mg g^{-1})	86.465	0.999	0.011	0.339	0.253	0.919
	K_2 (g mg^{-1} min^{-1})	0.095					
	h (mg g^{-1} min^{-1})	707.306					
	$t_{1/2}$ (min)	10.571					
Intraparticle diffusion	C (mg g^{-1})	55.1555	0.512	23.769	14.418	12.400	1663.136
	K_{id} (mg g^{-1} min$^{-0.5}$)	3.145					
Elovich	α (mg g^{-1} min^{-1})	1.33×10^{22}	0.999	0.256	1.648	1.456	21.73
	β (g mg^{-1})	0.633					

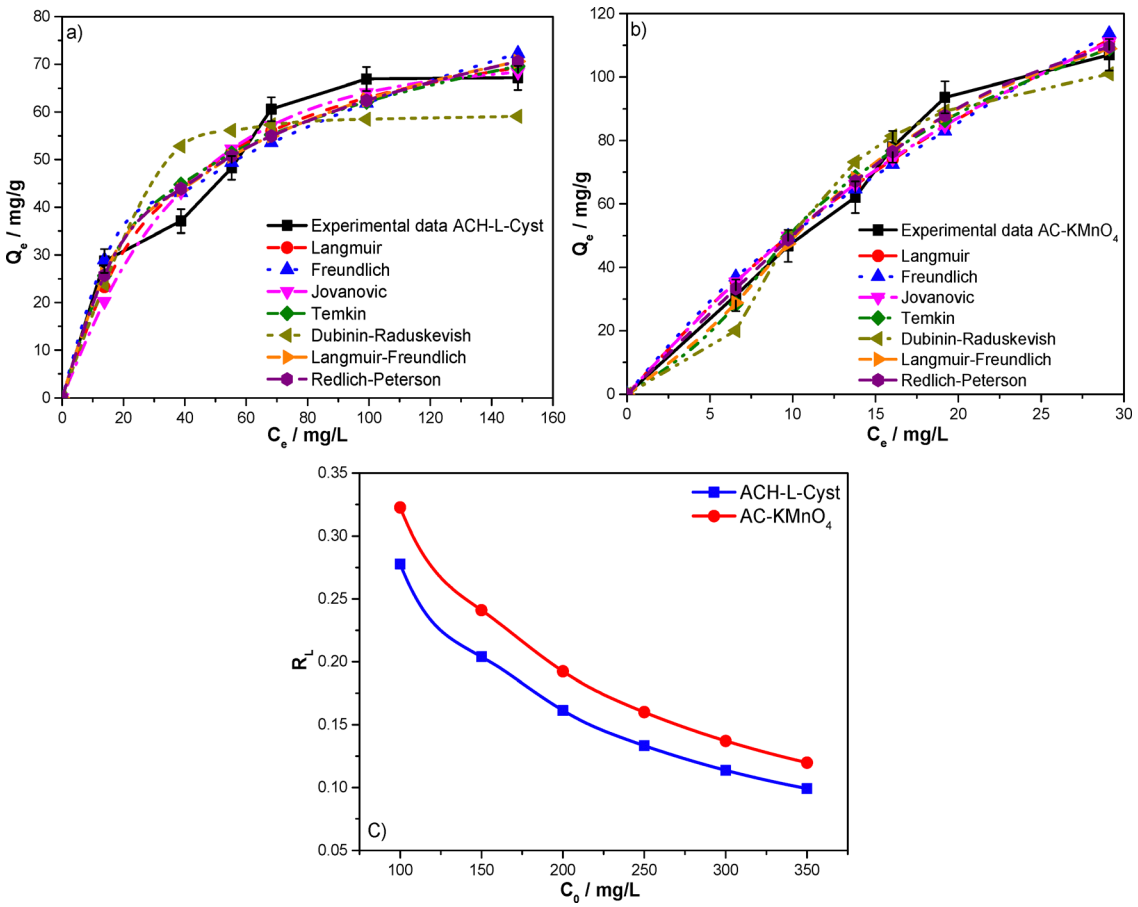

Fig. 12 Impact of concentration on the adsorption of Pb^{2+} ions, as well as adjusted non-linear experimental data for ACH-L-Cyst (a) and AC-$KMnO_4$ (b), Langmuir separation factor (c).

Table 5 Parameters of adsorption isotherms models

Models	Parameters	Values	R^2	χ^2	RMSE	ARE	SCE
ACH-L-Cyst							
Langmuir	Q_m (mg g^{-1})	86.882	0.963	2.618	4.687	5.706	131.857
	K_L (L mg^{-1})	0.0265					
Freundlich	K_F (L g^{-1})	10.571	0.961	2.87	4.811	5.744	138.871
	$1/n$	0.384					
Jovanovic	Q_m (mg g^{-1})	70.109	0.959	5.091	4.951	8.258	147.049
	K_J (L mg^{-1})	0.025					
Temkin	ΔQ (J mol^{-1})	134.156	0.962	2.849	4.759	5.178	135.882
	A (L g^{-1})	0.291					
Dubinin–Raduskevish	Q_m (mg g^{-1})	59.610	0.865	9.279	8.940	13.212	479.528
	β	30.401					
Langmuir–Freundlich	Q_{MLF} (mg g^{-1})	113	0.967	2.446	4.455	6.886	119.023
	M_{LF}	0.724					
	K_{LF}	0.044					
Redlich–Peterson	K_{RP} (L g^{-1})	3.624	0.964	2.606	4.607	7.201	125.763
	A_{RP} (L mg^{-1})	0.109					
	g	0.821					
AC-KMnO$_4$							
Langmuir	Q_m (mg g^{-1})	297.302	0.980	2.353	5.247	5.732	165.245
	K_L (L mg^{-1})	0.021					
Freundlich	K_F (L g^{-1})	8.949	0.971	3.367	6.282	6.727	236.838
	$1/n$	0.754					
Jovanovic	Q_m (mg g^{-1})	176.571	0.982	2.208	5.049	5.588	152.973
	K_J (L mg^{-1})	0.034					
Temkin	ΔQ (J mol^{-1})	45.762	0.986	1.695	4.368	4.574	114.481
	A (L g^{-1})	0.257					
Dubinin–Raduskevish	Q_m (mg g^{-1})	111.272	0.961	8.650	7.295	9.159	319.368
	β	13.896					
Langmuir–Freundlich	Q_{MLF} (mg g^{-1})	141	0.991	1.029	3.428	4.584	76.435
	M_{LF}	1.731					
	K_{LF}	0.00987					
Redlich–Peterson	K_{RP} (L g^{-1})	5.277	0.988	1.086	4.392	5.012	77.175
	A_{RP} (L mg^{-1})	3.883×10^{-4}					
	g	2.050					

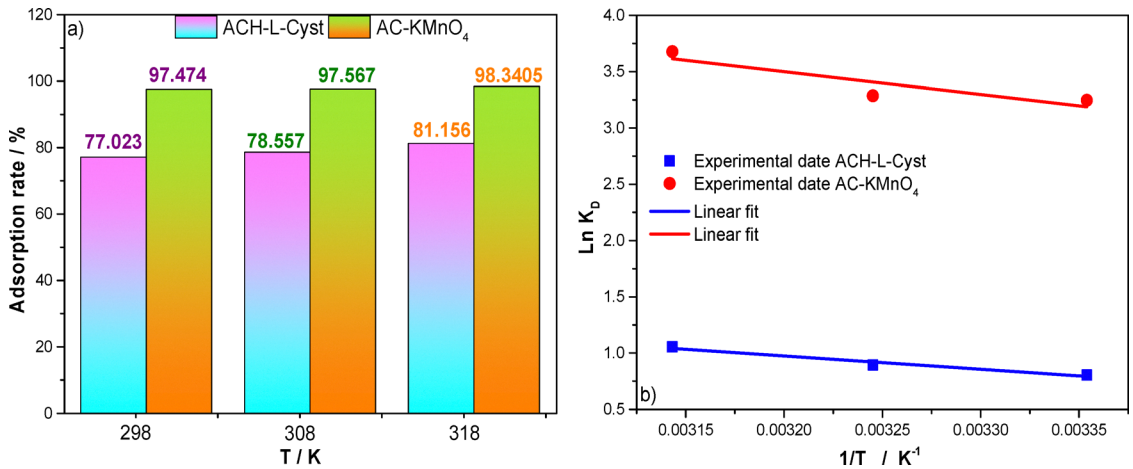

Fig. 13 Impact of temperature (a) and plot of ln K_D *versus* $1/T$ (b) of Pb adsorption on ACH-L-Cyst and AC-KMnO$_4$.

Lewis base of the two adsorbents can produce a more stable coordination compound.[69]

The distribution coefficient K_D (mL g^{-1}) is a factor that confirms the selectivity of an adsorbent towards the ions tested, which quantifies the adsorbent's ability to remove ions. Adsorption is considered excellent if the K_D value is greater than 1×10^4 mL g^{-1} (ref. 10 and 70) and a low α value indicates the affinity of the adsorbed metal for the adsorbents.[70] Analysis of Fig. 14b shows that adsorption is excellent for Pb^{2+}, Mg^{2+}, and In^{2+} ions with the AC-KMnO$_4$ adsorbent. However, with the ACH-L-Cyst adsorbent, adsorption is excellent with Pb^{2+} ions. The K_D value of AC-KMnO$_4$ and ACH-L-Cyst for Pb^{2+} ions is

Table 6 Thermodynamic parameters

	ΔG° (kJ mol^{-1})			ΔH°	ΔS°
	298.15 K	308.15 K	318.15 K	(kJ mol^{-1})	(J mol^{-1} K^{-1})
ACH-L-Cyst	−1.993	−2.287	−2.789	9.844	39.597
AC-$KMnO_4$	−7.903	−8.731	−9.558	16.766	82.742

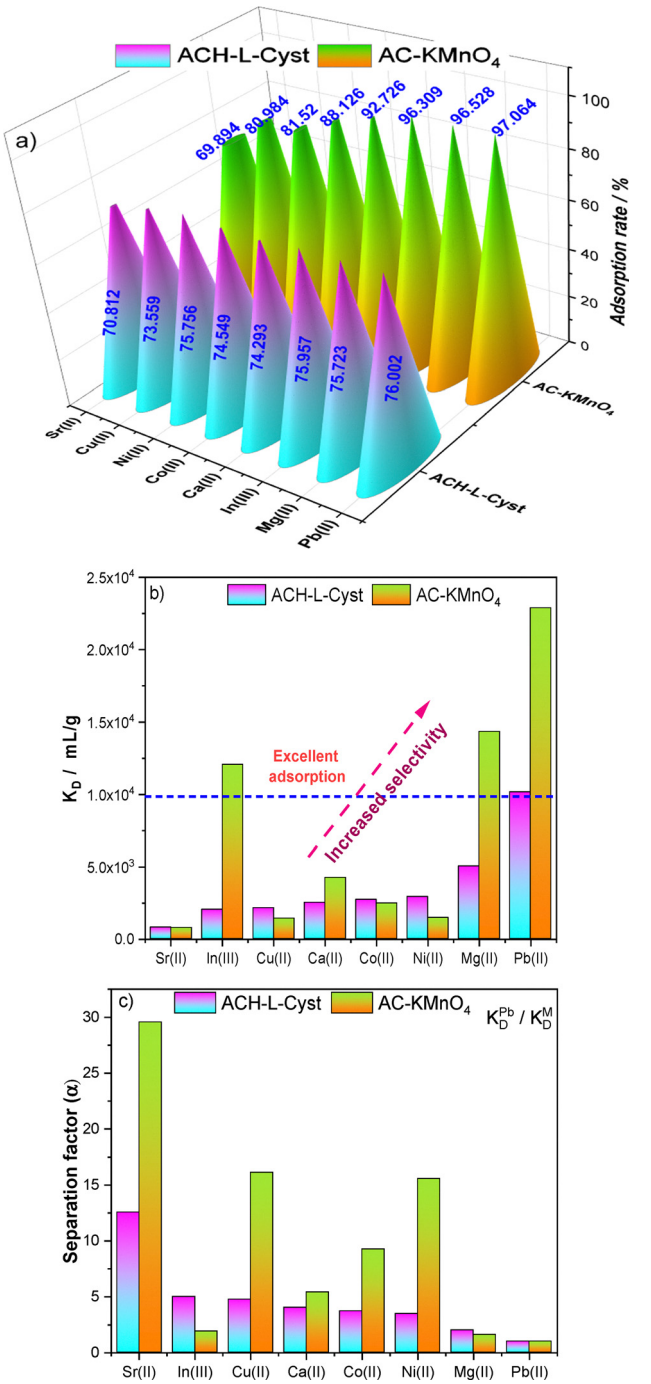

Fig. 14 Removal of various cations by ACH-L-Cyst and AC-$KMnO_4$ in ionic solutions containing a mixture of ions at an equal concentration of 210 mg L^{-1} (a), distribution coefficient (b) and separation factor (c).

much higher (K_D = 22 885.89 mL g^{-1} and 10 152.75 mL g^{-1}, respectively, for AC-$KMnO_4$ and ACH-L-Cyst), which confirms the high affinity of these two adsorbents for Pb^{2+} ions.

Although it allows the selectivity of an adsorbent towards a pollutant to be easily deduced, the distribution constant does not allow the competitive relationship between different ions in the same system to be established. Thus, in order to measure the adsorption affinity between the target ion and competing ions, an additional factor known as the separation factor or selectivity coefficient (α) is introduced.[71] Fig. 14c illustrates the various selectivity coefficients for each ion. It can be seen that AC-$KMnO_4$ has a strong affinity for Pb^{2+}, Mg^{2+}, and In^{2+} ions compared to other ions, while ACH-L-Cyst has a particularly strong affinity for Pb^{2+} ions, significantly higher than that for other ions.

3.2.7. Study of the reusability of adsorbents. As a general rule, two key factors, namely regeneration and structural stability, determine the practical application of adsorbents. The use of a strong acid is very useful for the desorption of pollutants. In this work, a mixture of distilled water and ethanol in a 50% volume ratio was used to regenerate spent ACH-L-Cyst and AC-$KMnO_4$. The stability of ACH-L-Cyst and AC-$KMnO_4$ as adsorbent materials for the removal of Pb^{2+} ions was evaluated through six consecutive adsorption test cycles carried out under optimal conditions. The outcomes are displayed in Fig. 15. This figure illustrates that the percentage of Pb^{2+} ion adsorption decreases as the number of regeneration cycles increases, falling from 77.002% to 59.4% for ACH-L-Cyst and from 97.473% to 66.971% for AC-$KMnO_4$. Table S9 shows the percentages of Pb^{2+} ion removal by the two adsorbents during the six cycles. The main reasons for the decrease in the removal rate by both adsorbents are probably the small amount of adsorbent lost during elution and the irreversible occupation of active adsorption sites.

3.2.8. Mechanism of adsorption. In order to clarify the adsorption mechanism, PXRD, FT-IR and SEM coupled with EDX/Mapping characterizations were performed to observe structural changes in ACH-L-Cyst and AC-$KMnO_4$ after Pb^{2+}

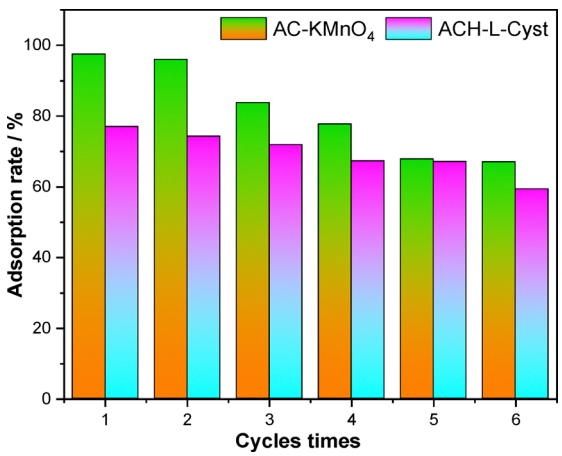

Fig. 15 Reusability of ACH-L-Cyst and AC-$KMnO_4$ for six consecutive cycles of adsorption–desoption.

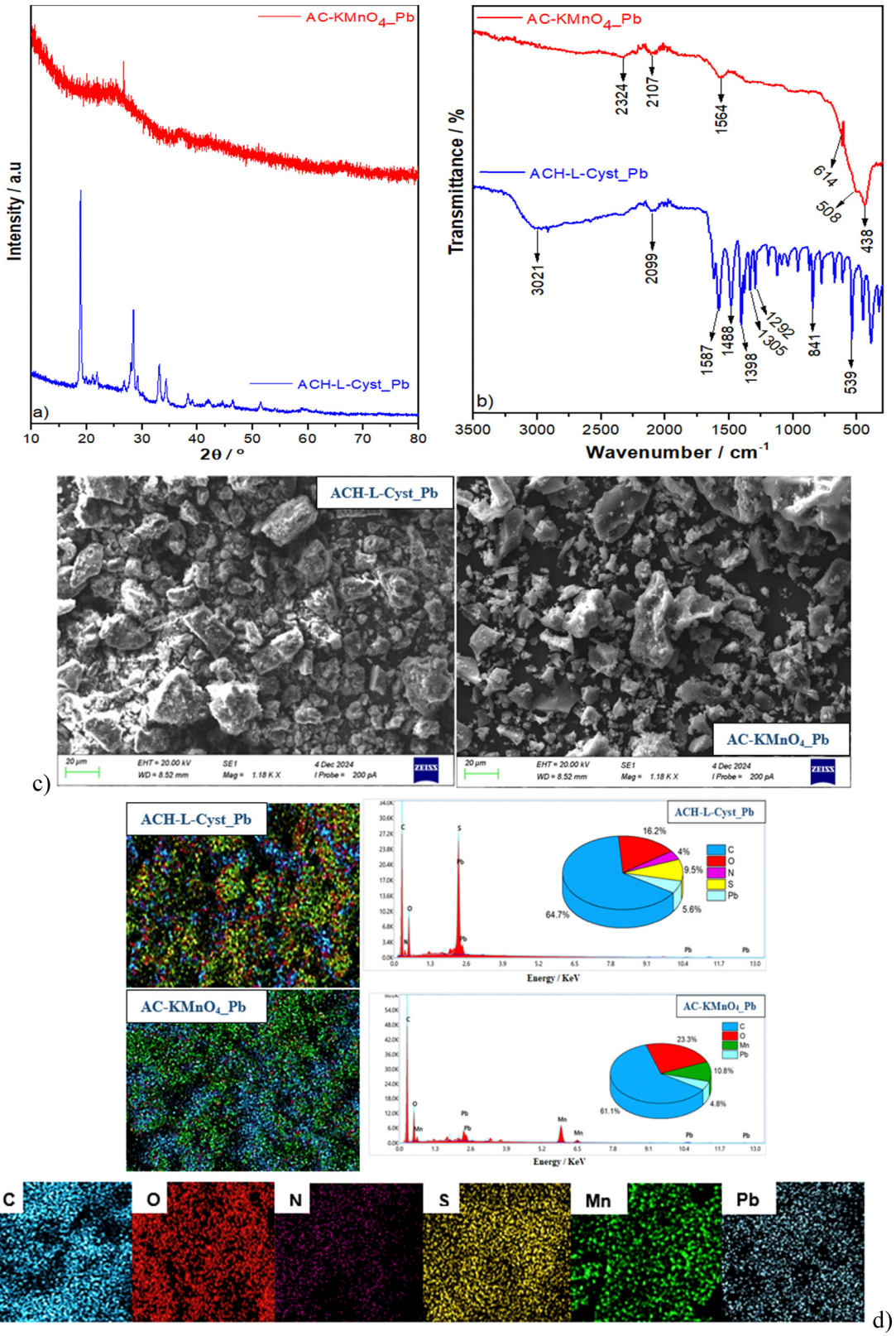

Fig. 16 (a) PXRD motif; (b) FT-IR spectra of ACH-L-Cyst and AC-$KMnO_4$ after Pb^{2+} adsorption; and (c) SEM/EDX-mapping of ACH-L-Cyst and AC-$KMnO_4$ after Pb^{2+} adsorption.

Table 7 A comparative study of Pb^{2+} ion adsorption by different adsorbents

Name of the adsorbents	Q_{max} (mg g^{-1})	Ref.
$KMnO_4$-modified bamboo biochar	123.47	3
Fly ash (FA)	75.3	25
TiO_2 modified fly ash (MFA)	62.7	25
Polyvinyl alcohol anchored-L-cysteine (PVA-L-CYS)	45.25	27
Chitosan-immobilised imino-phosphorane composite	55	28
Magnetic graphene oxide calcium alginate composite	270.27	29
L-Cysteine functionalized NH_2-MIL-53(Al)	38.01	30
Acid activated carbon doped with sulfur and nitrogen using L-cysteine (ACH-L-Cyst)	113	Present study
Activated carbon modified by hydrothermal oxidation using $KMnO_4$ (AC-$KMnO_4$)	141	Present study

adsorption. The PXRD pattern (Fig. 16a) shows identical reflections with the same crystal planes as for fresh ACH-L-Cyst and AC-$KMnO_4$ adsorbents, suggesting that no change in the crystal structure of these two adsorbents occurred as a result of the adsorption process, confirming the stability of the adsorbents. Fig. 16b shows the FT-IR spectra of ACH-L-Cyst and AC-$KMnO_4$ after adsorption. In general, the FT-IR spectra are similar, suggesting that the material after adsorption retains the same functions as the initial material. However, for the ACH-L-Cyst adsorbent, the shifts observed in certain stretching vibration peaks and the appearance of peaks at 1398, 1305, and 1292 cm^{-1} after adsorption of Pb^{2+} ions reflect the complexation of the latter with thiol groups (–SH), carboxylate groups ($–COO^-$), and amine groups ($–NH_2$). We can therefore say that the adsorption process is both physical and chemical in nature. For this adsorbent, the L-cysteine bound to the surface of the activated carbon acts as a chelating ligand to effectively capture Pb^{2+} ions by forming a stable surface complex. For the AC-$KMnO_4$ adsorbent, all of the stretching vibration peaks initially present in the FT-IR spectrum before adsorption are shifted. However, after adsorption of Pb^{2+} ions, a peak at 614 cm^{-1} attributed to stretching vibrations of the Pb–O bond in the PbO_2 crystal lattice appears. This band at 614 cm^{-1} is evidence that the adsorption of Pb^{2+} ions by $KMnO_4$-modified activated carbon is accompanied by oxidation at its surface. The SEM observation shown in Fig. 16c, compared to the sample before adsorption (Fig. 3), reveals the accumulation of lead on the surface of both adsorbents after adsorption. However, the image of the ACH-L-Cyst adsorbent after adsorption of Pb^{2+} ions shows that the adsorbent has been crushed, resulting in a final adsorbent with a fibrous structure. The changes observed in both adsorbents suggest, however, that the adsorption process mainly involves surface interactions, such as ion exchange or complexation for the ACH-L-Cyst adsorbent, and oxidation or precipitation for the AC-$KMnO_4$ adsorbent, rather than adsorption by infiltration and pore blocking.[3,56] They also indicate that the adsorption mechanism did not radically alter the morphology of the adsorbents. Fig. 16d shows the results of EDX mapping. These results confirm the presence of lead on the surface of ACH-L-Cyst and AC-$KMnO_4$, thus demonstrating the effective adsorption of lead(II) ions.

A comparative study of the maximum adsorption capacity of Pb^{2+} ions by the adsorbents in this study and some of those reported in the literature is presented in Table 7 below.

4. Conclusion

This study demonstrated the effectiveness of modified activated carbons doped with sulphur and nitrogen (ACH-L-Cyst), and oxidized by $KMnO_4$ (AC-$KMnO_4$), for the adsorption of Pb^{2+} ions in an aqueous medium. Structural and spectroscopic analyses confirmed the incorporation of the doping elements and an increase in the number of surface functional groups. Under optimal conditions, the adsorption efficiencies obtained were 77.20% and 97.22% for ACH-L-Cyst and AC-$KMnO_4$, respectively. Thermodynamic studies indicate an endothermic, spontaneous and favorable physisorption process. Despite a slight decrease in performance after several cycles, both adsorbents retain good reusability. The mechanisms involved are surface complexation, ion exchange and cation-π interactions, which confirm the high potential of these materials for treating wastewater contaminated with heavy metals.

Author contributions

Idris-Hermann Tiotsop Kuete: writing – original draft, visualization, validation, resources, methodology, investigation, formal analysis, data curation, conceptualization, writing – review & editing; Cyrille Ghislain Fotsop: methodology, characterization, data curation, formal analysis and investigation, writing – review & editing; Alexandra Lieb: validation, supervision, investigation, formal analysis, writing – review & editing. Franziska Scheffler: validation, supervision, resources, project administration, conceptualization.

Conflicts of interest

No conflicts of interest have been reported for this document.

Data availability

The data is available in the supplementary information (SI) section of the article. See DOI: https://doi.org/10.1039/d6ma00193a.

Acknowledgements

The authors gratefully acknowledge the financial support provided by the German Academic Exchange Service (DAAD). In

addition, the researchers would like to thank MSc Dougmouo Giscard for his assistance with the TGA measurements, Ms Inès Sauer for the PXRD analysis, and Dr Elias Kluth for his assistance with the Raman spectroscopy.

References

1 R. Singh and R. Bhateria, Optimization and experimental design of the Pb^{2+} adsorption process on a Nano-Fe_3O_4-Based adsorbent using the response surface methodology, *ACS Omega*, 2020, **5**(43), 28305–28318, DOI: 10.1021/acsomega.0c04284.

2 P. Kumar, S. Soo, M. Zhang, Y. Fai and K. Kim, Heavy metals in food crops: Health risks, fate, mechanisms, and management, *Environ. Int.*, 2019, **125**, 365–385, DOI: 10.1016/j.envint.2019.01.067.

3 H. Deng, *et al.*, Adsorption of Malachite Green and Pb^{2+} by $KMnO_4$-Modified Biochar: Insights and Mechanisms, *Sustainability*, 2022, **14**(14), 2040, DOI: 10.3390/su14042040.

4 H. Shanavaz, *et al.*, Applied Surface Science Advances Adsorptive removal of Pb^{2+} ions using stable imine linked covalent organic frameworks: A simulated and experimental studies, *Appl. Surf. Sci. Adv.*, 2023, **18**, 100502, DOI: 10.1016/j.apsadv.2023.100502.

5 R. Vílchez, C. Gómez-Silván, J. Purswani, J. González-López and B. Rodelas, Characterization of bacterial communities exposed to Cr(III) and Pb(II) in submerged fixed-bed biofilms for groundwater treatment, *Ecotoxicology*, 2011, **20**(4), 779–792, DOI: 10.1007/s10646-011-0629-x.

6 Z. Chen, X. Pan, H. Chen, Z. Lin and X. Guan, Investigation of lead (II) uptake by Bacillus thuringiensis 016, *World J. Microbiol. Biotechnol.*, 2015, **31**(11), 1729–1736, DOI: 10.1007/s11274-015-1923-1.

7 H. G. Zaman and L. B. R. Pendyala, Application in the optimization of Pb (II) adsorption by chitosan from produced water by using response surface methodology, *Int. J. Environ. Sci. Technol.*, 2023, **20**(1), 197–208, DOI: 10.1007/s13762-022-03927-0.

8 H. Hajjaoui, A. Soufi, M. Abdennouri, S. Qourzal and H. Tounsadi, Removal of cadmium ions by magnesium phosphate: Kinetics, isotherm, and mechanism studies Applied Surface Science Advances Removal of cadmium ions by magnesium phosphate: Kinetics, isotherm, and mechanism studies, *Appl. Surf. Sci. Adv.*, 2022, **9**, 100263, DOI: 10.1016/j.apsadv.2022.100263.

9 V. A. Online, The effective removal of Pb^{2+} by activated carbon fi bers modi fi ed by L -cysteine: exploration of kinetics, thermodynamics and mechanism, *RSC Adv.*, 2022, 20062–20073, DOI: 10.1039/d2ra01521h.

10 C. Ji, Y. Ren, H. Yu, M. Hua, L. Lv and W. Zhang, Highly efficient and selective Hg (II) removal from water by thiol-functionalized MOF-808: Kinetic and mechanism study, *Chem. Eng. J.*, 2022, **430**, 2021, DOI: 10.1016/j.cej.2021.132960.

11 T. S. Tessema, A. T. Adugna and M. Kamaraj, Removal of Pb (II) from Synthetic Solution and Paint Industry Wastewater Using Activated Carbon Derived from African Arrowroot (Canna indica) Stem, *Adv. Mater. Sci. Eng.*, 2020, **2020**(1), 8857451, DOI: 10.1155/2020/8857451.

12 I. H. Tiotsop Kuete, R. D. Tchuifon Tchuifon, A. Bopda, C. Sadeu Ngakou, G. N. A. Nche and S. Gabche Anagho, Adsorption of Indigo Carmine onto Chemically Activated Carbons Derived from the Cameroonian Agricultural Waste Garcinia cola Nut Shells and Desorption Studies, *J. Chem.*, 2022, **2022**(1), 1236621, DOI: 10.1155/2022/1236621.

13 G. T. Kenda, *et al.*, Green synthesis of magnetic biochars derived from biobased orange peel materials as sustainable heterogeneous catalytic supports for the Fenton process, *Arab. J. Chem.*, 2024, **17**(2), 105502, DOI: 10.1016/j.arabjc.2023.105502.

14 S. Chen, M. Zhong, H. W. S. Zhou, W. L. T. Wang and J. Li, Modified biochar derived from walnut shell, *Int. J. Environ. Sci. Technol.*, 2023, 1551–1568, DOI: 10.1007/s13762-022-04002-4.

15 S. S. Aloud, B. H. Hameed, M. F. M. Yusop, H. A. Alharbi, J. P. Giesy and K. D. Alotaibi, Adsorption of Pb^{2+} by activated carbon produced by Microwave-Assisted K_2CO_3 activation of date palm leaf sheath fibres, *Water*, 2023, **15**(22), 3905, DOI: 10.3390/w15223905.

16 S. G. Mokue Mafo, *et al.*, Low-cost magnetic carbons-based rubber seed husks materials for highly efficient removal for reactive black 5 and reactive blue 19 textile dyes from wastewater, *Int. J. Environ. Anal. Chem.*, 2023, **00**(00), 1–25, DOI: 10.1080/03067319.2023.2269857.

17 A. Z. Mekuiko, *et al.*, Tailoring activated carbons based cocoa pods lignocellulosic materials for Reactive blue 19 adsorption: optimization, adsorption isotherm and kinetic investigation, *Desalin. Water Treat.*, 2023, **300**, 144–157, DOI: 10.5004/dwt.2023.29708.

18 G. F. K. Nindjio, *et al.*, Lignocellulosic-Based Materials from Bean and Pistachio Pod Wastes for Dye-Contaminated Water Treatment: Optimization and Modeling of Indigo Carmine Sorption, *Polymers*, 2022, **14**(18), 3776, DOI: 10.3390/polym14183776.

19 N. G. Ndifor-Angwafor, *et al.*, Biosorption of amaranth red in aqueous solution onto treated and untreated lignocellulosic materials (pineapple peelings and coconut shells), *J. Mater. Environ. Sci.*, 2017, **8**(12), 4199–4212, DOI: 10.26872/jmes.2017.8.12.441.

20 Z. Yang, *et al.*, Ni, Co-Embedded MOF-Derived N-Doped Bimetallic Porous Carbon for Adsorption-Photocatalytic Degradation of Organic Dyes and Antibiotics, *ACS Omega*, 2024, **9**(10), 11356–11365, DOI: 10.1021/acsomega.3c07420.

21 M. Zhao, Z. Huang, S. Wang, L. Zhang and Y. Zhou, Energy, Environmental, and Catalysis Applications Design of L-Cysteine Functionalized UiO-66 MOFs for Selective Adsorption of Hg (II) in Aqueous Medium Faculty of Metallurgical and Energy Engineering, Kunming University of Science State Key Laboratory of Complex Nonferrous Metal Resources Clean Utilization, School of Textile Science and

Engineering, Wuhan Textile University, Wuhan National Local Joint Laboratory of Engineering Application of Microwave Energy, *ACS Appl. Mater. Interfaces*, 2019, **11**(50), 46973–46983, DOI: 10.1021/acsami.9b17508.

22 R. B. N. Lekene, *et al.*, High-quality low-cost activated carbon/chitosan biocomposite for effective removal of nitrate ions from aqueous solution: isotherm and kinetics studies, *Biomass Convers. Biorefin.*, 2023, 0123456789, DOI: 10.1007/s13399-023-04239-0.

23 L. A. Amola, T. Kamgaing, R. F. T. Tagne, C. D. Atemkeng, I. H. T. Kuete and S. G. Anagho, Optimized Removal of Hydroquinone and Resorcinol by Activated Carbon Based on Shea Residue (Vitellaria paradoxa): Thermodynamics, Adsorption Mechanism, Nonlinear Kinetics, and Isotherms, *J. Chem.*, 2022, **2022**(1), 1125877, DOI: 10.1155/2022/1125877.

24 A. Vakili, A. A. Zinatizadeh, Z. Rahimi, S. Zinadini, P. Mohammadi and S. Azizi, The impact of activation temperature and time on the characteristics and performance of agricultural waste-based activated carbons for removing dye and residual COD from wastewater, *J. Clean. Prod.*, 2023, **382**, 134899, DOI: 10.1016/j.jclepro.2022.134899.

25 K. Singh, A. Kumar, A. Kumar and A. Agarwal, Journal of Hazardous Materials Advances Fly ash and TiO 2 modified fly ash as adsorbing materials for removal of Cd (II) and Pb (II) from aqueous solutions, *J. Hazard. Mater. Adv.*, 2023, **10**, 100256, DOI: 10.1016/j.hazadv.2023.100256.

26 R. Gao, *et al.*, Science of the Total Environment High-efficiency removal capacities and quantitative sorption mechanisms of Pb by oxidized rape straw biochars, *Sci. Total Environ.*, 2020, **699**, 134262, DOI: 10.1016/j.scitotenv.2019.134262.

27 S. A. Mahmoud, B. M. Atia and M. Abdalla, Polyvinyl Alcohol-Conjugated L-Cysteine: A Novel Metal Pincer for Efficient Heavy Metal Ions Removal from Wastewater, *ChemistrySelect*, 2024, 202401169, DOI: 10.1002/slct.202401169.

28 A. M. Amin, *et al.*, Design and utilisation of a novel poly imino- phosphorane composite for the effective removal of Pb and Cr ions from contaminated water sources, *Int. J. Environ. Anal. Chem.*, 2025, **105**(18), 6387–6414, DOI: 10.1080/03067319.2024.2420827.

29 S. B. Malitha, D. M. Mahmudunnabi, S. Mazumder, K. S. Hossain, M. Nurnabi and M. Z. Alam, Rapid adsorptive removal of Pb^{2+} ions from aqueous systems using a magnetic graphene oxide calcium alginate composite: optimisation, isotherms, and kinetics, *Environ. Sci. Adv.*, 2024, **4**(4), 595–605, DOI: 10.1039/d4va00341a.

30 B. Han, X. Xiao, L. Zhang, Y. Li, D. Wang and W. Ni, L-Cysteine functionalized NH 2 -MIL-53 (Al) for Pb 2p and Ni 2p removal from aqueous solution, *JCIS Open*, 2021, **1**, 100003, DOI: 10.1016/j.jciso.2021.100003.

31 S. Razzaq, *et al.*, Adsorption removal of Congo red onto L-cysteine/rGO/PANI nanocomposite: equilibrium, kinetics and thermodynamic studies, *J. Taibah Univ. Sci.*, 2021, 3655, DOI: 10.1080/16583655.2021.1876351.

32 H. Wang, S. Zang, H. Teng, X. Wang, J. Xu and L. Sheng, Characteristic of $KMnO_4$ - modified corn straw biochar and its application in constructed wetland to treat city tail water, *Environ. Sci. Pollut. Res.*, 2023, **30**(17), 49948–49962, DOI: 10.1007/s11356-023-25856-2.

33 X. Yang, *et al.*, Facile preparation of L-cysteine – modified cellulose microspheres as a low-cost adsorbent for selective and efficient adsorption of Au (III) from the aqueous solution, *Environ. Sci. Pollut. Res.*, 2020, 38334.

34 S. Sun, *et al.*, Adsorption of crystal violet on activated bamboo fiber powder from water: preparation, characterization, kinetics and isotherms, *RSC Adv.*, 2023, **13**(9), 6108–6123, DOI: 10.1039/d2ra08323j.

35 B. Li, J. Hu, H. Xiong and Y. Xiao, Application and Properties of Microporous Carbons Activated by ZnCl 2: Adsorption Behavior and Activation Mechanism, *ACS Omega*, 2020, **5**(16), 9398–9407, DOI: 10.1021/acsomega.0c00461.

36 Y. Zheng, *et al.*, Insight into the KOH/KMnO4 activation mechanism of oxygen-enriched hierarchical porous biochar derived from biomass waste by in-situ pyrolysis for methylene blue enhanced adsorption, *J. Anal. Appl. Pyrolysis*, 2021, **158**, 105269, DOI: 10.1016/j.jaap.2021.105269.

37 H. Kim and N. Saito, One-pot synthesis of purple carbon hybrids and synergistic enhancement for the removal of cationic dyes, *Sci. Rep.*, 2018, **2017**, 1–13, DOI: 10.1038/s41598-018-22203-1.

38 M. Moheb, A. M. El-wakil and F. S. Awad, RSC Advances papaya plant (stems and leaves) for superior dyes from wastewater, *RSC Adv.*, 2025, **15**, 674–687, DOI: 10.1039/D4RA07957D.

39 S. Mopoung and T. Bunterm, $KMnO_4$ Modified Carbon Prepared from Waste of Pineapple Leaf Fiber Production Processing for Removal of Ferric Ion from Aqueous Solution, *Am. J. Appl. Sci.*, 2016, **13**(6), 814–826, DOI: 10.3844/ajassp.2016.814.826.

40 G. Tan, Y. Liu and D. Xiao, Preparation of manganese oxides coated porous carbon and its application for lead ion removal, *Carbohydr. Polym.*, 2019, **219**, 306–315, DOI: 10.1016/j.carbpol.2019.04.058.

41 S. Harabi, S. Guiza, Á. Ariadna, G. Almudena and M. Bagan, Adsorption of Pesticides on Activated Carbons from Peach Stones, *Processes*, 2024, 238.

42 K. Le Van, T. Thuy and L. Thi, Activated carbon derived from rice husk by NaOH activation and its application in supercapacitor, *Prog. Nat. Sci. Mater. Int.*, 2014, **24**(3), 191–198, DOI: 10.1016/j.pnsc.2014.05.012.

43 M. F. K. Pyrzyńska and A. B. P. Pietrowski, Improved adsorption performance of activated carbon covalently functionalised with sulphur - containing ligands in the removal of cadmium from aqueous solutions, *Int. J. Environ. Sci. Technol.*, 2019, 0123456789, DOI: 10.1007/s13762-019-02398-0.

44 J. Gonzalez, I. Dossou, L. Helene, S. Jensen and J. Peña, Contaminant loading and competitive access of Pb, Zn and Mn (III) to vacancy sites in biogenic MnO_2, *Chem. Geol.*, 2018, **502**, 76–87, DOI: 10.1016/j.chemgeo.2018.10.020.

45 M. A. Sarran, A. A. Abdulrazak, M. F. Abid and A. D. Jawad, Activated Iraqi bentonite, *Desalin. Water Treat.*, 2024, **319**, 100412, DOI: 10.1016/j.dwt.2024.100412.
46 C. G. Fotsop, A. Lieb and F. Scheffler, Tailoring the water vapor adsorption properties by thermal performance analysis of post-synthetically ion-exchanged LTA zeolite derived from Cameroonian kaolin, *J. Ind. Eng. Chem.*, 2025, **155**, 683–698, DOI: 10.1016/j.jiec.2025.08.017.
47 K. Lucresse, *et al.*, Unraveling the sorption mechanism of industrial dyes onto Zr-based MOFs: computational and removal, *Mater. Adv.*, 2024, 16–19, DOI: 10.1039/D4MA00818A.
48 C. Equilibrium, T. Studies, A. H. Birniwa, R. Edrees, A. Mohammad and M. Ali, Synthesis of Gum Arabic Magnetic Nanoparticles for Adsorptive Removal of Synthesis of Gum Arabic Magnetic Nanoparticles for Adsorptive Removal of Ciprofloxacin: Equilibrium, Kinetic, Thermodynamics Studies, and Optimization by Response Surface Methodology, *Separations*, 2022, 322, DOI: 10.3390/separations9100322.
49 M. R. Fathi, H. R. Noormohamadi, M. Ghaedi and G. R. Ghezelbash, Optimizing the biosorption of Bi^{3+} ions by Streptomyces rimosus using experimental design and applicability in kinetics and isotherm modeling, *RSC Adv.*, 2016, **6**(46), 40287–40295, DOI: 10.1039/c6ra03513b.
50 F. Shehab, A. May, A. Alsaffar and A. Abduljabbar, One - step synthesis of magnetic fly ash composites for methylene blue removal: batch and column study, *Environ. Sci. Pollut. Res.*, 2022, 0123456789, DOI: 10.1007/s11356-022-23491-x.
51 J. Mao, M. Ge, J. Huang and Y. Lai, Constructing multifunctional MOF@rGO hydro-/aerogels by the self-assembly process for customized water remediation, *J. Mater. Chem. A*, 2017, 11873–11881, DOI: 10.1039/c7ta01343d.
52 X. Yang, Y. Wan, Y. Zheng, F. He, Z. Yu and J. Huang, Surface functional groups of carbon-based adsorbents and their roles in the removal of heavy metals from aqueous solutions: A critical review, *Chem. Eng. J.*, 2019, **366**, 608–621, DOI: 10.1016/j.cej.2019.02.119.
53 Z. Lingkai, X. Man, Y. Yuyuan and L. Ping, Thiol -functionalized activated carbon fibers as efficient adsorbents, *Mater. Chem. Phys.*, 2023, **302**, 127552, DOI: 10.1016/j.matchemphys.2023.127552.
54 C. G. Fotsop, A. Lieb and F. Scheffler, Core-satellite material based metal-doped zeolite LTA for highly efficient iodine sequestration: Adsorption performance and mechanism, *Inorg. Chem. Commun.*, 2026, **183**(P1), 115742, DOI: 10.1016/j.inoche.2025.115742.
55 M. Zbair, RSC Advances Reusable bentonite clay: modelling and optimization of hazardous lead and p -nitrophenol adsorption using a response surface methodology approach, *RSC Adv.*, 2019, **9**, 5756–5769, DOI: 10.1039/C9RA00079H.
56 A. El-Rayyes, *et al.*, Thermodynamic, isotherm and kinetic studies lead ions adsorption onto Manihot esculenta chaff surface, *Sci. Rep.*, 2025, **15**(1), 27672, DOI: 10.1038/s41598-025-09307-1.
57 M. I. Shaukat, R. Wahi and Z. Ngaini, Bio - based activated carbon for Cu(II), Ni(II), and Pb(II) ions aqueous sequestration: physiochemical characterization, isotherms, and kinetics, *Int. J. Environ. Sci. Technol.*, 2024, **22**(5), 3763–3786, DOI: 10.1007/s13762-024-05856-6.
58 N. Khan, F. Wahid, Q. Sultana, N. Us and S. Muhammad, Surface oxidized and un - oxidized activated carbon derived from Ziziphus jujube Stem, and its application in removal of Cd (II) and Pb (II) from aqueous media, *SN Appl. Sci.*, 2020, **2**(4), 1–11, DOI: 10.1007/s42452-020-2578-6.
59 A. Reda, A. El-Demerdash, W. Sadik, E. El-Rafey and T. Shoeib, Effectively eliminating lead and cadmium from industrial wastewater using a biowaste-based sorbent, *Appl. Water Sci.*, 2025, **15**(2), DOI: 10.1007/s13201-024-02343-8.
60 C. S. Ngakou, G. S. Anagho and H. M. Ngomo, Non-linear Regression Analysis for the Adsorption Kinetics and Equilibrium Isotherm of Phenacetin onto Activated Carbons, *Curr. J. Appl. Sci. Technol.*, 2019, **36**(4), 1–18, DOI: 10.9734/CJAST/2019/v36i430246.
61 D. Raoul, T. Tchuifon, G. N. Ndifor-angwafor, A. Bopda and S. Gabche, Modeling of phenol adsorption isotherm onto activated carbon by non-linear regression methods: models with three and four parameters, *Desalin. Water Treat.*, 2018, **136**, 199–206, DOI: 10.5004/dwt.2018.22898.
62 I.-H. T. Kuete, D. R. T. Tchuifon, G. N. Ndifor-Angwafor, A. T. Kamdem and S. G. Anagho, Kinetic, Isotherm and Thermodynamic Studies of the Adsorption of Thymol Blue onto Powdered Activated Carbons from Garcinia cola Nut Shells Impregnated with H_3PO_4 and KOH: Non-Linear Regression Analysis, *J. Encapsulation Adsorpt. Sci.*, 2020, **10**(01), 1–27, DOI: 10.4236/jeas.2020.101001.
63 C. G. Fotsop, A. Lieb and F. Scheffler, Applied Surface Science Advances Insights into the synergistic effects of ZnO/MgO and Zn/Mg-modified porous zeolite as core-satellite materials for tuning water vapor sorption properties, *Appl. Surf. Sci. Adv.*, 2025, **30**, 100855, DOI: 10.1016/j.apsadv.2025.100855.
64 D. Alvine Loris, *et al.*, Kinetic and Isotherm Studies of the Adsorption Phenacetin onto Two Copper Porous Coordination Compounds: Nonlinear Regression Analysis, *J. Chem.*, 2022, 2022, DOI: 10.1155/2022/2828860.
65 C. G. Fotsop, A. Lieb and F. Scheffler, Core-shell material based on ion-exchange-assisted growth of ZIFs on chamfered-edged zeolite crystals for N_2/CO_2 adsorption: Modeling and mechanism, *J. Environ. Chem. Eng.*, 2025, **13**(6), 119887, DOI: 10.1016/j.jece.2025.119887.
66 M. Bansal, B. Ram, G. S. Chauhan and A. Kaushik, L-Cysteine functionalized bagasse cellulose nanofibers for mercury(II) ions adsorption, *Int. J. Biol. Macromol.*, 2018, **112**, 728–736, DOI: 10.1016/j.ijbiomac.2018.01.206.
67 I. El-Hallag, A. Al-Owais and E. El-Mossalamy, Kinetic and thermodynamic investigation of the removal of alizarin red dye using silica- supported nanoscale zero-valent iron

particles, *Sci. Rep.*, 2025, **15**(1), 31461, DOI: 10.1038/s41598-025-15233-z.

68 T. Wajima and K. Sugawara, Adsorption behaviors of mercury from aqueous solution using sulfur-impregnated adsorbent developed from coal Mixing with K_2S, *Fuel Process. Technol.*, 2011, **92**(7), 1322–1327, DOI: 10.1016/j.fuproc.2011.02.008.

69 Y. Liu, *et al.*, Study on the synthesis of poly(pyrrole methane)s with the hydroxyl in different substituent position and their selective adsorption for Pb^{2+}, *Chem. Eng. J.*, 2018, **361**, 528–537, DOI: 10.1016/j.cej.2018.12.093.

70 C. G. Fotsop, A. Lieb and F. Scheffler, Highly efficient removal and separation of Sr^{2+}, Co^{2+}, In^{3+} and Ni^{2+} in single and mixed ion systems on low-cost Zeolite, and its stability analysis: DFT and experimental investigations, *Chem. Eng. J. Adv.*, 2025, **25**, 100986, DOI: 10.1016/j.ceja.2025.100986.

71 L. N. Pincus, *et al.*, Exploring the Mechanisms of Selectivity for Environmentally Significant Oxo-anion Removal During Water Treatment: a Review of Common Competing Oxo-anions and Tools for Quantifying Selective Adsorption, *Environ. Sci. Tech.*, 2020, **54**(16), 9769–9790, DOI: 10.1021/acs.est.0c01666.